Rotation and Turbulence in Peripheral Heavy Ion Collisions

Dujuan Wang

Dissertation for the degree philosophiae doctor (PhD)

at the University of Bergen

2014

Dissertation date: December 16, 2014

Contact: Dujuan Wang

Departments of Physics and Technology

University of Bergen

Allégaten 55

5007 Bergen

Norway

Email: azaleawdj@gmail.com

Acknowledgements

Three and a half years passed even before I realized it. It was like I just came to Bergen while now it's time to submit my PhD thesis. This reminds me the first time I met my supervisor Prof. László P. Csernai on April 27, 2011, just several days before my master's thesis defense in Central China Normal University. At that time I was very shy partly due to my oral English, which needed urgent improvements. He was so kind that he spoke slowly and explained to me in more details whenever I could not follow. This is what he has been doing in the following years also. He encourages me and gives me help whenever I need it, not only about the research problems but also many trivial things in my daily life. He led me to the field of fluid dynamics in heavy ion physics with comprehensive insights and profound knowledge background and he taught me how to deal with things systematically and effectively. I am inspired by his enthusiasm and tremendous interests in doing research. Only with his selfless and continuous help, his valuable ideals and critical comments, I can complete my doctoral study here.

I owe special thanks to Prof. Xu Cai in Central China Normal University. He guided me to the fantastic and desirable palace of physics when I was an undergraduate. I would like to show my great gratitude to him for his selfless and continuous support and help during these years.

I would like to thank Prof. Jan S. Vaagen and Prof. Dieter Röhrich for their help and encouragements during my stay here. I would like to thank Prof. Marcus Bleicher for his kind hospitality during my stay in Frankfurt Institute for Advanced Studies (FIAS), it was an important semester of my PhD studies. I appreciate the fruitful discussions

with Prof. Daniel Strottman, Prof. Horst Stöcker, Prof. Zoltan Néda, Prof. Francesco Becattini, Prof. Tamás Csörg, Prof. Volodymyr Magas and Prof. Larissa Bravina. Thanks very much for all your contributions of time, ideas and helpful comments.

I would like to thank the senior consultant, Terje Finnekås, for many help and encouragements during my study here.

I wish to express my warm and sincere thanks to Prof. Benhao Sa for his valuable suggestions and encouragements. I appreciate his serious attitude and clear logics when discussing research problems. I am grateful to Prof. Daimei Zhou, Dr. Yun Chen and Dr. Yuliang Yan for their useful comments, discussions and kind help.

Grateful thanks are given to my friends and colleagues in Bergen, Lijiao Liu, Meidana Huang, Zhuo Zhou, Lei Chen, Jesper Tveit, Astrid Marie Skålvik, Sindre Velle, Sedat Altinpinar, Eirik Hatlen, Yilong Xie and Shengxin Zhao, you made my life in Bergen colorful and fantastic, I am happy to be with all of you.

Special thanks go to Bianca Ross, I am so lucky to meet her. She is so gracious whenever I see her. Thank you for inviting me to the several dinners with magical cooking and also for your care and encouragement.

Special thanks go to Agnes Csilla Till for driving me home each time when I fly back from a conference, and also for the nice dinners during the years. I will always remember your encouragement that whenever you meet something which looks quite hard, never say its impossible but instead say yes I will try it.

I would like to express my deepest gratitude to my parents, sisters and brothers. Thank you for giving me a warm and beloved family. You are the light of my life that inspires me to struggle and move forward. I owe particular thanks to my husband, Dr. Weibing Deng, he always encourages me whenever I meet a problem and helps me find confidence to confront all the difficulties. Thanks for your continuous patience and understanding.

Abstract

In our computational fluid dynamics (CFD) calculations the Kelvin-Helmholtz instability (KHI) starts to develop in peripheral collisions. At high energies the shear viscosity of the Quark Gluon Plasma (QGP) flow is becoming small and the Reynolds number will exceed one, thus turbulent phenomena may start to occur, which enhance the rotation effect in the expanding system. Due to the large initial state angular momentum, a new directed flow structure may appear that the anti-flow peak observed at high energies rotates forward, and directed flow will start to peak at positive rapidities at sufficiently high beam energy, i.e. on the same side where the projectile spectator residues arrive after the collision. This is because the initial angular momentum leads to a faster rotating initial system, and this rotation moves the dominant directed flow peak forward before the expansion from the pressure which would slow down the rotation. The observation of this peak is not easy because of the beam directed fluctuations of the initial state, and the directed flow is very sensitive and subject to significant perturbations from these random fluctuations. Thus we can study other effects, which are induced by the rotation of the expanding system. One is the polarization method: by calculating the thermal vorticity it turns out that the Lambda polarization can reach several percent in peripheral heavy ion collisions. The other is the Differential Hanbury Brown Twiss method, which is sensitive to rotation and it has advantages compared with the flow harmonics analysis.

Contents

Chapter 1

Introduction

The early universe is produced after a Big Bang and it is filled with hot dense matter. After a few milliseconds, this extraordinary hot and dense matter is composed by a fundamental form of matter, the Quark Gluon Plasma (QGP), behaving like a soup, with the matter moving almost at the speed of light. The field theory, the Quantum Chromodynamics (QCD), can describe these quanta and leads to the conclusion that the quarks and gluons are confined by strong interaction. They do not live for long time and recombine into ordinary hadronic matter moving in every direction, thus it can not be easily detected in laboratory. It is assumed that the light produced in the early universe can reach us thus we can observe it. This makes the cosmic microwave background (CMB) studies of the thermal radiation possible. This year the polarization measurement of the Cosmic Microwave Background radiation were reported by the Amundsen-Scott South Pole Station. The observed circular polarization (the so called B-mode polarization), the existence of which has been long predicted, paves the way for a definitive test of inflation (a key theory in the Big Bang model of the universe). It is thought to be the consequence of gravitational waves ("large ripples" in space-time) formed at the early explosion of the "inflationary" universe. The CMB fluctuations, however, are dependent on past events, and we can try to recreate similar conditions and generate hot dense matter by ultra-relativistic heavy ion collision experiments. We can make the nuclei

collide head on and the matter may melt into QGP, then it cools instantly and plenty of particles will be produced at these high energy collisions. The particles which are flying towards the detectors can be detected and recorded. These observed particles contain the information about the QGP.

With increasing energies, the collective flow phenomena become increasingly dominant, the multiplicity of final state particles is already several thousands after the collisions, which makes the produced particles behave more like a continuum, and the Fluid Dynamic approach can be used to study the heavy ion collisions. With the QGP production confirmed in RHIC and LHC, the scope of the fluid dynamical studies is widening, and at the same time their application becomes more dominant in recent years. The advances in the collective flow studies have a wide spread of directions. Due to the low viscosity of QGP near to the phase-transition threshold, both significant (i) fluctuations and (ii) new Global Collective instabilities may occur, as turbulence in peripheral reactions, which is the main research subject of this thesis. The precise analysis of these two types of effects would require both their theoretical study and their experimental separation, and then their possible interaction and interference in the observables. The necessity of this separation is pointed out and elaborated in more detail in this thesis.

In Fluid Dynamic model it is important to use a realistic 3+1D initial states, which can describe realistically the early evolution of the collision without unrealistic simplifying assumptions, for example, all symmetries of a heavy ion reaction should be reflected in Global Collective initial state. However this is usually not considered in the initial state, as in numerous fluid dynamical models the x, y, η, τ coordinates are used, thus it is easy to assume uniform longitudinal Bjorken scaling flow, so that $v_\eta = 0$. This is frequently done even in 3+1D models, which immediately eliminates the longitudinal shear flow, thus the arising vorticity. Once the longitudinal momentum distribution is assumed to be uniform in the transverse plane, or if it is assumed to be symmetric around the collision's z-axis, the initial angular momentum will be lost, which violates the conservation of angular momentum and also disables the description of many fundamental

phenomena. There are few realizations where the conservation laws are fully satisfied.

For a realistic model, the initial state (in terms of z, t or η, τ) should have longitudinal ends, which do not exceed the projectile and target rapidities, rather we should take into account the effects of the recoil and deceleration caused by the other colliding nucleus. The initial state can be generated from a realistic molecular dynamics or cascade model, which may reach states close to equilibrium, then the smooth average of such states can serve as a realistic 3+1D initial state. In fact a good analytic initial state can be constructed by taking into account all symmetries and all conserved quantities and their conservation laws. Such realistic initial state can be used as an input for our Particle in Cell (PIC) hydrodynamic model for numerical simulation of the collision, where the space is divided into many cells, i, and each cell is filled with particles which are randomly generated following the distribution function $f(x_i, p)$. The number of cells filled with matter increases as the system evolves and expands until the pressure approaches zero, thus many cells in the center of space may became empty. The energy and net particle numbers are conserved during the expansion.

Structure of the thesis

This thesis is written on the basis of 7 published papers [1, 2, 3, 4, 5, 6, 7] and 5 conference proceedings [8, 9, 10, 11, 12] which are included in Appendix F. The other Appendices are important parts of the thesis, which provide some details (not shown in the published papers) necessary for the publications.

There are six chapters of the thesis. Chapter 2 introduces the theoretical fundamentals including the Particle in Cell hydrodynamical model and the initial state, then the measurables and the freeze out are also mentioned.

Chapters 3, 4 and 5 are brief introductions and summaries of my publications:

Chapter 3 (publications [7, 9]): Fluctuations from random initial conditions, not from the phase-transition are shown in this part. The higher moments, the skewness and

kurtosis changes sign both with and without the phase-transition. The global collective flow and fluctuations can be separated by the azimuthal harmonics method.

Chapter 4 (publications [1, 2, 5, 6]): The rotation effect is predicted by our FD model where the Kelvin Helmholtz Instability (KHI) is observed, this effect can lead to the flow vorticity. The conditions for development of KHI are investigated analytically and the rate of slowing down rotation is studied in an extended solution of the FD model.

Chapter 5 (publications [3, 4]): It is important to find some evidence that the exploding system is rotating. In our FD calculation the Λ polarization observation for higher and intermediate energy collision as well as the two particle Differential Correlation Function (DCF) are introduced to detect rotation.

The conclusion and outlook are given in chapter 6.

Importance and innovative features of the topic of the thesis

This thesis studies a new collective flow pattern, the KHI and the rotation due to the large angular momentum for peripheral high energy collisions. This angular momentum is a very important property for heavy ion collisions, however it is usually ignored up to now. Thus these studies are very new.

In our work we take into account the big angular momentum by using a realistic initial state model, where the participant zone is divided into streaks characterized by the string tension. The momentum of the streaks varies and the most peripheral streaks near the spectators contribute the most to the angular momentum.

The KHI is very sensitive to the viscosity thus it can be used to measure the QGP viscosity in heavy ion collisions as shown in the thesis. One typical phenomenon induced by the rotation is the vorticity, thus we also study it for peripheral collisions and its value is impressive. Since the rotation and radial expansion of the fluid compete with each other, for high energy collisions the antiflow peak might rotate forward and become

positive at positive rapidity, this is more obvious for higher and for more peripheral collisions.

All these features are innovative in the study of this field. The strong dependence of the occurrence of the KHI from the viscosity (which is expected to have a minimum at the phase-transition to QGP) makes these studies very important as a specific direct signal of the minimum of viscosity and at the phase-transition threshold at the same time.

Chapter 2

Theoretical fundamentals

This chapter is based on the textbook "Introduction to Relativistic Heavy Ion Collisions" [13].

2.1 Notations and conventions

We work in natural units where $c = \hbar = 1$. At high energy systems the relativistic approach describes the dynamics of the variables better, thus we use the conventions at special relativity which are repeated here.

2.1.1 Phase space variables

The space time coordinates take into account the time, t, in addition to the normal spatial (x,y,z)-coordinates, thus it constructs a four dimensional space-time, which is spanned by the coordinates $x^\mu = (t, x, y, z) = (t, \boldsymbol{r})$. Here x^μ is a contravariant 4-vector. The four vector with a superscript is called contravariant and the subscripted ones are covariant, i.e., the covariant space-time vector is x_μ. The contravariant and covariant variables can be can be transformed to each other by the action of the metric tensor, which takes the form $g_{\mu\nu} = g^{\mu\nu} = diag(1, -1, -1, -1)$, thus $x_\mu = g_{\mu\nu}x^\nu$.

In relativity the Lorentz contraction should be considered, thus the contravariant

four velocity is $u^\mu = (\gamma, \gamma\boldsymbol{v})$ and the covariant four velocity is $u_\mu = (\gamma, -\gamma\boldsymbol{v})$, where $\boldsymbol{v}$ is three spatial velocity components and $\gamma = 1/\sqrt{1-\boldsymbol{v}^2}$ is Lorentz contraction factor. The 4-velocity is a time-like unit vector pointing to the moving direction of a particle since it has the norm $u^\mu u_\mu = 1$. When we mention about time-like, we mean a quantity characterized by a 4-vector should be similar to the 4-velocity of the matter in the space-time which is spanned by the time coordinate and lightcone. A four vector, q^μ, is time-like when $q_\mu q^\mu > 0$ and space-like when $q_\mu q^\mu < 0$. For a unit four vector Λ^μ, if $\Lambda^\mu\Lambda_\mu = 1$, it is time-like and if $\Lambda^\mu\Lambda_\mu = -1$ then it is space-like. The time-like and space-like four vectors can not be transformed to each other by Lorentz transformation.

The **four momentum** is $p^\mu = (p^0, \boldsymbol{p})$, here $p^0 = \sqrt{(\boldsymbol{p})^2 + m^2}$ is relativistic energy of a moving particle, $\boldsymbol{p}$ is 3-momentum in the space. This 4-momentum is time-like because $p^\mu p_\mu = (p^0)^2 - (\boldsymbol{p})^2 = m^2$. The three velocity is defined as $\boldsymbol{v} \equiv \boldsymbol{p}/p^0$.

Usually in heavy ion physics we denote the z component of a vector by subscript $||$ and the other ones by $\perp$, i.e., the three velocity is $\boldsymbol{v} = (v_{||}, \boldsymbol{v}_\perp)$, thus the four velocity is $u^\mu = \gamma(1, v_{||}, \boldsymbol{v}_\perp)$. Similarly the momentum vector is $p^\mu = (p^0, p_{||}, \boldsymbol{p}_\perp)$.

2.1.2 Rapidity

Rapidity is an alternative measure of the motion speed, it is defined as

$$y \equiv \mathrm{arcth}\boldsymbol{v}_{||} = \mathrm{arcth}\frac{p_{||}}{p^0} = \frac{1}{2}\ln\frac{p^0 + \mathrm{p}_{||}}{p^0 - p_{||}} \ ,$$

it is proportional to the velocity for small velocities, $y \approx v_{||}$. The rapidity can better describe the kinetic motion of particles, as the energies of the system increase, the rapidity can take the values from $-\infty$ to ∞, unlike the velocity, which can only approach the light velocity c. Another important property is that the rapidity is additive. If a particle in frame K_1 has rapidity y_1 and at the same time the frame K_1 is moving at rapidity y_2 in frame K_2, then the particle has the rapidity $y = y_1 + y_2$ in K_2 frame. This is the Lorentz transformation property of rapidity.

In experiment it is difficult to measure the particle energy directly, the pseudorapidity η is defined in terms of the momentum:

$$\eta = \frac{1}{2}\ln\frac{|\boldsymbol{p}| + p_{||}}{|\boldsymbol{p}| - p_{||}} \ .$$

At ultra high energy the mass energy mc^2 is negligible, the energy $p^0 = \sqrt{\boldsymbol{p}^2 + m^2} \approx |\boldsymbol{p}|$, thus the rapidity and pseudorapidity are equal $y \approx \eta = \ln(\cot\frac{\theta}{2})$, where θ is the polar angle between the momentum and the beam axis.

2.1.3 Particle four flow

Particle 4 flow $N^\mu = (\mathsf{n}(x), \boldsymbol{j}(x))$ is a macroscopic quantity, which is composed by the local density $\mathsf{n}(t, \boldsymbol{r}) = \mathsf{n}(x)$ and the local particle flow $\boldsymbol{j} = \boldsymbol{j}(t, \boldsymbol{r}) = \boldsymbol{j}(x)$, where x is the space time coordinate.

The local density and the local particle flow can be expressed in terms of the particle distribution function, $f(x, p)$, in a given reference frame:

$$\mathsf{n}(x) = \int d^3p \ f(x,p) \ , \tag{2.1}$$

$$\boldsymbol{j}(x) = \int d^3p \ \boldsymbol{v} \ f(x,p) \ , \tag{2.2}$$

where the particle distribution is a probability function, which can be used to calculate the particle number in μ space, i.e., in a 6 dimensional (x,p) space, the number of particles in a phase space element is $\Delta N = f(x,p)\Delta^3 x \Delta^3 p$. Since $\boldsymbol{v} = \boldsymbol{p}/p^0$, the Eqs. (2.1, 2.2) can take a general form

$$N^\mu = \int \frac{d^3p}{p^0} \ p^\mu \ f(x,p) \ , \tag{2.3}$$

here N^μ and p^μ are both 4-vector, thus $\int \frac{d^3p}{p^0} \ f(x,p)$ should be an invariant scalar.

2.1.4 Energy momentum tensor

The energy momentum tensor describes the energy density and flux of energy and momentum in space-time:

$$T^{\mu\nu}(x) = \int \frac{d^3p}{p^0}\ p^\mu\ p^\nu\ f(x,p)\ . \tag{2.4}$$

It has the components of the energy density $T^{00}(x)$, the energy flow T^{0i}, the momentum density T^{i0} and the momentum flow tensor T^{ik}, where i and k take the values of 1, 2 and 3. The energy momentum tensor can be considered as the second order moment of particle function $f(x,p)$. It is symmetric since $T^{\mu\nu} = T^{\nu\mu}$. It includes the rest mass and the kinetic energy of the particles while it does not include the fields and potential energy.

2.1.5 Local Rest Frame (LR)

The word line is a trajectories of a particle moving in 4 dimensional space time coordinates, the flow velocity u^μ is a time like vector tangent to the world line of the particle when there are particles in the matter. If there are no particles, the flow velocity is parallel to the energy flow. These two types of flow will be shown via two definitions later.

A four vector in n dimensional space can be projected orthogonally to the flow velocity u^μ into a hypersuface which has $n-1$ dimensions by the action of the projector $\Delta^{\mu\nu}$:

$$\Delta^{\mu\nu} \equiv g^{\mu\nu} - \frac{u^\mu u^\nu}{(u^\nu u_\nu)}\ , \tag{2.5}$$

it is apparent that this projector acting on the flow velocity is 0 ($\Delta^{\mu\nu}u_\mu = 0$). If the flow velocity in some frame is $u^\mu = (1,0,0,0)$, this frame is called the Local Rest frame (LR) with flow velocity $u^\mu_{(\mathrm{LR})}$. In this frame we have $\Delta^{\mu\nu}_{(\mathrm{LR})} = \Delta_{\mu\nu\ (\mathrm{LR})} = diag\ (0,-1,-1,-1)$ and $\Delta^{\mu}_{\nu\ (\mathrm{LR})} = diag\ (0,1,1,1)$.

The invariant scalar density is the density in the Local Rest frame $n \equiv N^\mu u_\mu = N^0_{(\mathrm{LR})}$.

This density is different from the previous introduced local density n, which is not an invariant scalar. They are equal only when we are in Local Rest frame. The invariant scalar energy density, $e \equiv u_\mu T^{\mu\nu} u_\nu$, is $T^{00}_{(\mathrm{LR})}$ in the Local Rest frame. The pressure tensor can be calculated by using the orthogonal projector, which is defined as $P^{\mu\nu} \equiv \Delta^\mu_\sigma T^{\sigma\tau} \Delta^\nu_\tau$. In the Local Rest frame we have $P^{00}_{(\mathrm{LR})} = P^{i0}_{(\mathrm{LR})} = P^{0i}_{(\mathrm{LR})} = 0$ and $P^{ij}_{(\mathrm{LR})} = T^{ij}_{(\mathrm{LR})}$ for $i, j = 1, 2, 3$. In fact one can find more invariant scalar densities in the Local Rest frame, i.e., $(p^\mu u_\mu)_{(\mathrm{LR})} = p^0 = E$. Such invariant scalar is the same in all other reference frames.

The Local Rest frame can be obtained by performing a Lorentz transformation since u^μ is a time-like vector. There are two ways to find the Local Rest frame by introducing Eckart's definition and Landau's definition:

Eckart's definition

In this definition the Local Rest frame can be obtained by the help of the particle 4-flow N^μ indicating there are conserved particles or charges in the flow. In this case the unit vector of flow velocity is

$$u^\mu = \frac{N^\mu}{(N^\nu N_\nu)^{1/2}} \ , \tag{2.6}$$

thus the flow has the spatial 3-velocity $\boldsymbol{v}$ parallel to the particle current $\boldsymbol{j}$ since $u^\mu = \gamma(1, \boldsymbol{v})$. In this case the projector acting on the flow is 0 ($\Delta_{\mu\nu} N^\mu = 0$) and it eliminates the spatial particle flow in its Local Rest frame

$$N^i_{(\mathrm{LR})} = 0; \ i \ = \ 1, 2, 3 \ ,$$

which means the particle four flow is $N^\mu = (n(x), 0, 0, 0)$. This definition does not work for coherent flow systems with particles and antiparticles, which will yield vanishing particle flow. It is not suitable for low baryon density system because the mass and energy flow will be independent of the vanishing particle flow. Thus for ultra-relativistic heavy ion collisions it is ill defined since the system would have very high energy density and very low or zero baryon density.

Landau's definition

In this definition the Local Rest frame is tied to energy flow 4 vector where the spatial components of energy flow $T^{0i}_{(\mathrm{LR})}$ and the momentum density $T^{i0}_{(\mathrm{LR})}$ $(i = 1, 2, 3)$ should vanish. By assuming the flow velocity parallel to the energy flow $T^{\mu\nu}u_\nu$, according to Eq. (2.5), we have

$$\Delta_{\sigma\mu}T^{\mu\nu}u_\nu = 0 \ .$$

Since $\Delta_{\mu\nu}$ is an orthogonal projector, the flow velocity u^μ is a normalized eigenvector of $T^{\mu\nu}$ and $u^\mu = constant \times T^{\mu\nu}u_\nu$, where the constant$= (u_\sigma T^{\rho\nu}u_\nu)^{-1}$.

2.2 Hydrodynamical model

Fluid dynamical processes can be used to describe heavy ion reactions in all energy regions and it becomes a dominant direction of research in high energy heavy ion reactions in recent years. With increasing energies, the hadron multiplicity grows up to thousands, thus the matter generated is behaving more and more like a continuum. This makes the fluid dynamic approach more realistic by assuming the matter reaching local thermodynamic equilibrium and satisfying the conservation laws. The equation of fluid dynamics are the conservation equations of particle and energy:

$$N^\mu{}_{,\mu} = 0 \text{ or } \partial_\mu(nu^\mu) = 0 \ , \tag{2.7}$$

$$T^{\mu\nu}{}_{,\mu} = 0 \text{ or } \partial_\mu(T^{\mu\nu}) = 0 \ , \tag{2.8}$$

where the notation $,_\mu$ has the form $,_\mu \equiv \frac{\partial}{\partial x^\mu} \equiv \partial_\mu \equiv (\partial_t, \nabla \boldsymbol{r})$. For ideal fluids the energy momentum tensor is

$$T^{\mu\nu} = (e + P)u^\mu u^\nu - Pg^{\mu\nu} \ .$$

thus we have $T^{ik} = \omega\gamma^2 v_i v_k + P\delta_{ik}$, $T^{0i} = -T_{0i} = \omega\gamma^2 v_i$ and $T^{00} = T_{00} = (e + Pv^2)\gamma^2$ where $\omega = e + P$. Here we can introduce the momentum current density $\mathcal{M} \equiv T^{0i}$ and

the apparent energy density $\mathcal{E} \equiv T^{00}$. The apparent density can also be introduced as $\mathcal{N} \equiv n\gamma = \mathsf{n}$. By using these three quantities, the fluid dynamic equations take the more familiar form:

$$\partial_t \mathcal{N} + \nabla \cdot (\boldsymbol{v}\mathcal{N}) = 0 \ , \tag{2.9}$$

$$\partial_t \boldsymbol{\mathcal{M}} + \nabla \cdot (\boldsymbol{v}\boldsymbol{\mathcal{M}}) = -\nabla P \ , \tag{2.10}$$

$$\partial_t \mathcal{E} + \nabla \cdot (\boldsymbol{v}\mathcal{E}) = -\nabla \cdot (P\boldsymbol{v}) \ . \tag{2.11}$$

Here Eq. (2.9) is the continuity equation, Eq. (2.10) and Eq. (2.11) are Euler equation of fluid dynamics and the energy conservation. These fluid dynamic equations can be solved numerically with an Equation of State (EOS): $P = P(n, T)$ or $P = P(n, e)$.

2.2.1 Relativistic Boltzmann Transport Equation

To obtain the fluid dynamic Eqs. (2.9, 2.10, 2.11) one needs the particle distribution function $f(x, p)$. If we do not consider an external force and the particles do not collide, the relativistic transport equation is $p^\mu \partial_\mu f(x, p) = 0$. The Relativistic Boltzmann Transport Equation (BTE) takes into account two particle (binary) collisions and assumes that the number of binary collisions at x is proportional to $f(x, p_1) \times f(x, p_2)$. Collisions among particles change the particle distribution function. If two particles collide at position x, their initial momentum p and p_1 change to final momentum p' and p_1', the Relativistic Boltzmann transport equation is:

$$p^\mu \partial_\mu f(x, p) = \frac{1}{2} \int \frac{d^3 p_1}{p_1^0} \frac{d^3 p'}{p'^0} \frac{d^3 p_1'}{p_1'^0} [f' f_1' W(p', p_1'|p, p_1) - f f_1 W(p, p_1|p', p_1')] \ ,$$

where $W(p, p_1|p', p_1')$ is the transition rate depending only on momentum p. The factor $\frac{1}{2}$ is introduced due to symmetric when we exchange $p, p_1 \leftrightarrow p_1', p'$. We have the notation $f \equiv f(x, p)$, $f' \equiv f(x, p')$, $f_1 \equiv f(x, p_1)$ and $f_1' \equiv f(x, p_1')$.

2.2.2 Jüttner distribution

The Jüttner distribution is the stationary solution of the Relativistic BTE which can be used in perfect fluid dynamic equations. It has the form:

$$f^{Jüttner}(p) = \frac{1}{(2\pi\hbar)^3} \exp \frac{\mu(x) - p^\nu u_\nu(x)}{T} \ . \tag{2.12}$$

where μ is the chemical potential, T is temperature. In Local Rest frame $(p^\nu u_\nu)_{\mathrm{LR}} = (p^0)_{\mathrm{LR}} = E$, and it is the same in all other reference frame since it is an invariant scalar. But p^0 is the time component of a 4-vector, thus it is not an invariant scalar. If $f(x,p)$ is a stationary solution of BTE, it should be $f^{Jüttner}(x,p)$. Most of the time the local particle distribution $f(x,p)$ is close to $f^{Jüttner}$ since the equilibrium stage can be reached very fast.

2.2.3 The Particle in Cell (PIC) method

The PIC method is used as a tool for numerical simulation to solve a certain class of partial differential equations. In this calculation we divide the space into grid cells and one grid cell is denoted by i, j, k. The relations between these indexes and the spatial coordinates $\boldsymbol{x}$ are shown in Appendix A. Each cell contains many randomly generated particles according to the particle distribution function.

There are basicly two approaches to solve the fluid dynamic equations, the Eulerian method and the Lagrangian method. The Eulerian grid is fixed in space and accounts for the storage of momentum, energy and particles. The fluid can move across these grid cells thus the number of cells filled with matter is increasing as the system is expanding. On the other hand the Lagrangian mesh cells move with the fluid, thus the fluid does not flow in or out of these cells. The Marker Particles in the PIC method are such Lagrangian cells.

The equations are solved in two steps. The first step is the Lagrangian phase where the Lagrangian fluid cells distort and follow the fluid, which means the grid and particles

move together, thus the transport parts between neighboring Lagrangian cells in Eqs. (2.9,2.10,2.11) can be ignored.

In the second step we need to consider the transport properties between the bigger Eulerian cells. The cell momentum and energy are distributed evenly among all the particles in this Eulerian cell thus each Marker Particle (=Lagrangian cell) has an effective velocity, $\overline{v}_{i,j,k}$. In δt time each Marker Particle moves a distance $\overline{v}_{i,j,k}\delta t$. After a movement if the Marker Particle remains in the same cell, the energy and momentum of this Eulerian cell does not change; If it crosses the Eulerian cell boundary, the momentum and energy carried by this marker particle should be added to its new Eulerian cell and subtracted from the old one.

2.3 Initial stage of collisions

Computational fluid dynamic models are widely used to describe heavy ion reactions, the EoS can vary flexibly and can test the corresponding dynamic results. However, the initial and final freeze out stages are outside the applicability of the fluid dynamical model, thus an energetic heavy ion reaction requires a Multi Module Model to describe the collision process more realistically, where the different stages can be studied by a suitable theoretical approach. For hadronization and freeze out stages, the matter is very dilute and can be well described by kinetic models, thus it is more important to deal with the initial stage. This thesis uses the initial state developed in [14] where the system is tilted for noncentral collisions. This initial state is in fact essential for large initial angular momentum and leads to the KHI and rotation effect in hydrodynamical calculations.

2.4 Freeze out and measurable quantities

The hydrodynamical model can simulate the collision and calculate the measurables, which can be used to compare with the experimental data. In hydrodynamics the par-

ticles generated may keep interacting as long as they become dilute and independent, however, this is not the case in experiments where the particles reaching the detectors have not interact for a long time already. Thus it is important to break up the interaction in the hydrodynamical model, which needs the freeze out process. A gradual freeze out and hadronization process can be handled in fluid dynamics assuming phase equilibrium but it takes a long time, thus a sudden freeze out process is used in our calculation to describe the freeze out process.

2.4.1 The freeze out process

The freeze out process can be usually replaced by a sudden freeze out where a hypersurface can be introduced in space-time. The particles interact according to fluid dynamical laws before the matter reaches this surface. Once this surface is reached, the continuum becomes independent particles where final interactions and collisions are neglected among these particles. Usually we refer this surface pre-freeze out surface before crossing and post-freeze out surface after crossing.

For one surface we calculate the entropy on both sides and make sure it does not decrease otherwise another FO hypersurface is needed. On this surface, the conservation laws should be satisfied, namely the particle 4-current N^μ and the the energy-momentum tensor $T_{\mu\nu}$ should satisfy the ralations

$$[N^\mu d\sigma_\mu] = 0 \ , \ [T^{\mu\nu} d\sigma_\mu] = 0 \ , \ [s^\mu d\sigma_\mu] \geq 0 \ ,$$

where $[a] = a_2 - a_1$ is the change of a quantity a across the hypersurface. The brackets mean the conservation of a given quantity since the four current N^μ and energy momentum tensor $T^{\mu\nu}$ are not continuous across the surface, but they can be calculated from the total particle number, energy and momentum which should always be the same on both sides.

The flow velocity will also change if its direction is not parallel to the freeze out

surface normal ($d\sigma^\mu$). This modifies the freeze out method of Cooper and Frye [15] because even if the direction is the same as the surface normal but with different EoS, the parameters of post-freeze out matter will also change, such as the temperature, since the particle interaction energy should be added to the kinetic energy of noninteracting particles [16].

2.4.2 The measurables

The measurables can be calculated from the particle distribution function after the FO hypersurface. The experimental measurables are usually differential quantities normalized per event, such as the quantity

$$\frac{dN}{d^3p}$$

should satisfy the normalization

$$N = \int_S \frac{dN}{d^3p} d^3p = \int_S \left(\int \frac{d^3p}{p^0} p^\mu f_0(x,p) \right) d\sigma_\mu = \int_S n(x) u^\mu d\sigma_\mu \ , \tag{2.13}$$

where f_0 is the ideal gas phase space distribution including collective flow. The overall quantities can be calculated by the help of the particle number, such as the momentum of emitted particles, which is frequently measured in experiments. The transverse momentum in Reaction Plane is

$$p^x_{tot} = \int_S \frac{dN}{d^3p} p^x d^3p = \int_S \left(\int \frac{d^3p}{p^0} p^\mu p^x f_0(x,p) \right) d\sigma_\mu = \int_S T^{\mu x} d\sigma_\mu \ . \tag{2.14}$$

We usually use the assumption $u^\mu = d\sigma^\mu$ in analytic models where spherical or cylindrical symmetry is assumed, since this assumption can simplify the above equations.

Some most common measurables are the the baryon and pion measurables. The local baryon momentum space distribution assumes the Jüttner distribution, and the

pion distribution assumes a Relativistic Bose distribution:

$$f_\pi(x,p) = \frac{g_\pi}{(2\pi\hbar)^3} \frac{1}{\exp\frac{p^\mu u_\mu}{T} - 1} \ .$$

In both cases there are several measurables, such as rapidity distribution $\frac{dN_{\rm cell}}{dy}$, the transverse momentum spectra $\frac{dN_{\rm cell}}{p_\perp dp_\perp}$, see more details in [13].

It is important to mention that in Eqs. (2.13, 2.14), the post freeze out phase space distribution of particles $f(x,p)$ should not include particles which propagate backwards into the mater not freeze out yet. To avoid these "negative contributions" one should use the cut Jüttner [17] or canceling Jüttner [18, 19] distributions as post freeze out distributions.

Chapter 3

Collective flow and fluctuations

Collective flow has been measured and azimuthal asymmetry was determined from v_1 to v_8 in heavy ion reactions. The fluctuating initial configuration is the main source for flow fluctuations in central collisions at high energies and the most dominant flow harmonic is v_3. These collective flow fluctuations have no direct connection to the fluctuations which arise from a phase-transition in the Equation of State (EoS) [20, 21, 22, 23]. In our 3+1D fluid dynamical model we study the dynamical development of expanding Quark-gluon Plasma (QGP) flow for central collisions where the fluctuations are minimized by using the azimuthally symmetric initial state. Then we present a method to split the two flow patterns, the collective flow and the fluctuations.

3.1 Higher moments of QGP flow

The fluctuations arising from the pure fluid dynamics are studied in [7] without including any effect associated with a phases transition in the EoS, in the transport properties, or in special thermodynamical phase space trajectories [24, 25, 26], or in special freeze out mechanisms. Ref. [27] studied the critical fluctuations generated from QGP phase to hadronic phase and included a first order transition, while in Ref. [7] we complement a large number of studies with the opposite goal, aiming to analyze the consequences of the statistical properties when the phase-transition is not assumed and the matter undergoes

a supercooling process. The higher moments for extensive densities are calculated such as skewness and kurtosis, to see what kind of effects the conservative relativistic fluid dynamical model would exhibit.

We choose the MIT Bag model with parameters fixed to the initial values which includes two flavors and massless quarks and gluons. We use the simplest bag model approach, which is in the pure QGP domain, yields similar results to more detailed parametrizations fitted to lattice predictions [28]. The bag constant is $B = 0.397$ GeV$/fm^3$ for positive pressure, while for originally negative pressure fluid cells we change the bag constant to a smaller value in order to get zero pressure and nondecreasing entropy, see more details in Appendix B. This is necessary since the zero pressure cells are a big part of the fluid at late stages in our fluid dynamic model, see Fig. 3.1.

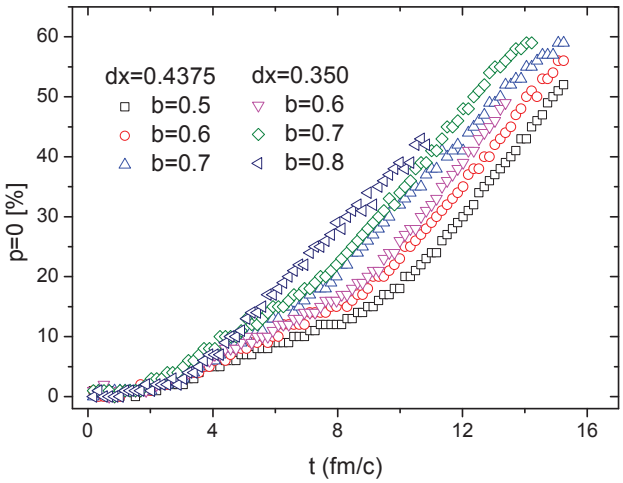

Figure 3.1: The percentage of the fluid cells with vanishing pressure as a function of time, impact parameter and the cell size, calculated by the hydro code. Up to the typical freeze out time of 5-8 fm/c, the pressure is zero in more than 15% of the fluid cells.

The viscosity is not considered (except the unavoidable numerical viscosity) in order to omit its effects, thus neither the temperature dependence of viscosity near the critical point [29] is considered, which may lead to additional changes of the critical fluctuations in a viscous fluid dynamical evolution. The dimensionless shear viscosity over the entropy density, η/s, of the QGP is becoming small [30] at high energies and η/s as a function of

temperature has a minimum at the critical temperature [31]. On the other hand, η/s at a critical point does not necessarily have a minimum, since the dynamical universality class of a possible critical point of QCD is the H-model in Hohenberg and Halperin's classification [32, 33], the shear viscosity may diverge at a possible QCD critical point which would damp instabilities. Since the turbulence and instability appears only for small viscosity indicating the critical point of the matter [31], it is a sensitive measure of viscosity and its minimum at the critical point. The observed high flow harmonics directly indicate a low viscosity and the lack of viscous damping.

The description of the final stage of the reaction is needed for a realistic reaction model. We have a Multi Module Model approach to describe high energy heavy ion collisions in the RHIC and LHC energy range. From the locally equilibrated QGP we have to form hadrons. We do not assume that the hadronization happens in chemical equilibrium since this would take too long time [34] and would not allow for baryons of high strangeness. Thus, we assume a fast, non-equilibrium hadronization and freeze out based on Cooper-Frye method, with a local sudden change, or a sudden transition to a parton and hadron cascade model, e.g. [35], which can describe rapid hadronization without the assumption of chemical equilibration. This final stage would increase the deviations from the local statistical equilibrium additionally. The final calculated particle distribution, which contains the influence of the rapid hadronization and freeze out, should be compared to the basic fluctuations arising from a (least fluctuating) CFD distribution estimate.

We first study the trajectory of fluid dynamical development of QGP fluid at different beam energies for central collisions, see Fig. 1 in Ref. [7]. As a result the CFD evolution is calculated well beyond hadronic freeze out curve [36]. This is possible because the PIC Relativistic (PICR) model can well describe supercooled QGP fluid. In fact our fluid calculation can be performed down to FAIR and NICA energies where the supercool QGP EoS has constrained validity.

Then the higher moments are calculated in this CFD model by using the Particle in

Cell model containing N fluid cells. With time development and expansion the number of fluid cells is increasing, thus the baryon charge per cell is less and less. Therefore we weight a quantity x of the fluid cells by the amount of baryon charge they carry:

$$< x >\equiv \sum_i x_i \cdot w_i \ , \quad w_i = \frac{\mathsf{n}_i^{\rm CF} \cdot V_i}{N_{tot}} \ , \tag{3.1}$$

where w_i is the weight, V_i is the volume of i^{th} fluid cell, $\mathsf{n}_i^{\rm CF}$ is the baryon density in the Calculational Frame (CF), which is the c.m. frame in the present calculations. The baryon density in CF and in Local Rest Frame have the relation $\mathsf{n}_i^{\rm CF} = n_i^{\rm LR}\gamma_i$, so that $N_{tot} = \sum_i n_i^{\rm LR}\gamma_i V_i$, thus the weight is normalized to 1 ($\sum_i w_i = 1$). The average of a variable x to $n^{\rm th}$ order is $< x^n >= \int x^n P(x)dx = \sum_i x_i^n \ w_i$, where $P(x)$ is the spatial distribution weighted by the baryon charge density in the CF, thus the moments can be calculated as:

$$M^{(n)} =< (x- < x >)^n >= \int (x- < x >)^n P(x)dx = \sum_i (x- < x >)^n \ w_i \ , \tag{3.2}$$

where $M^{(2)}$ is the square of spatial variance (σ^2), $\frac{M^{(3)}}{(M^{(2)})^{3/2}}$ is the skewness (S) and $\frac{M^{(4)}}{(M^{(2)})^2} - 3$ is the kurtosis (κ). Usually most random fluctuations may lead to Gaussian distribution while the dominant fluid dynamical expansion may lead to more complex non-gaussian fluctuations and higher statistical moments even if all special sources are eliminated or minimized.

We study the higher moments of different thermodynamical parameters (especially intensives and extensives) since they do not show the same critical fluctuation properties, such as the energy density, the baryon charge density, etc. The developments of average energy densities and baryon densities as well as their variances show an expected, monotonic dynamical behavior, even beyond the physical FO times, where we overstretched the applicability of the fluid dynamical model.

However the Kurtosis and Skewness show a non monotonic behavior, in order words the Kurtosis and Skewness of specific energy densities change signs during the time

development, although we have applied the least questionable EoS for the highest energy collisions and we do not include critical fluctuations generated from rapid hadronization in our FD model. This means the spatial fluctuations of energy density and baryon charge density certainly influence the final baryon charge multiplicity and specific energy distributions. In addition different initial states and initial state fluctuations may also influence the thermodynamical parameters. Thus, the effects of the FD expansion and of the final hadronization and freeze out should be separated. This can be done in theoretical hybrid models by analyzing the effects from all stages of the reaction dynamics separately or more specific correlation measurements.

3.2 Splitting of collective flow and fluctuations

In hydrodynamical calculations the peak position of v_1 Global flow moves to "forward" rapidities with increasing beam energy and initial angular momentum. This is a result of our tilted initial state with shear flow [14], in which the angular momentum from the increasing beam momentum may supersede the expansion driven by the pressure, see Fig. 3.2. Our CFD simulations suggest that we can measure the collective directed flow function $v_1(y)$ if the Globally asymmetric flow component and the random flow arising from the initial state fluctuations are separated. The center of mass rapidity can be affected by initial state fluctuations since the participant nucleon numbers from projectile and target are not exactly the same event-by-event. These fluctuations have two reasons [37]: (i) the unfixed position of a particle in the participant plane, and (ii) the particles in the participant zone not always become participants since they may not collide.

The collective global flow in noncentral collisions has the form:

$$\frac{d^3N}{dydp_td\phi} = \frac{1}{2\pi}\frac{d^2N}{dydp_t}\left[1 + 2v_1(y,p_t)\cos(\phi) + 2v_2(y,p_t)\cos(2\phi)\right] \ .$$

where y is the rapidity and ϕ is the azimuthal angle in the transverse plane with respect

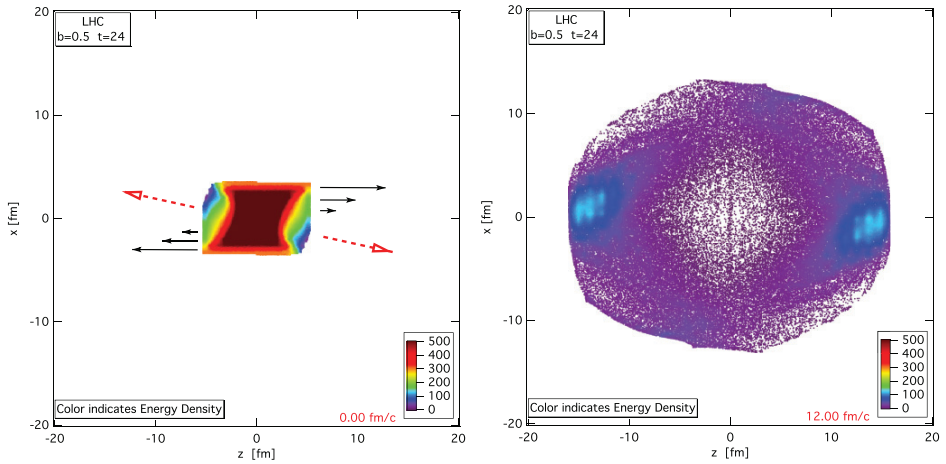

Figure 3.2: (Color online) The energy density (GeV/fm^3) distribution at time 4 fm/c after impact (left) (when the fluid dynamical calculation starts) and at time 12 fm/c after hydro initial state formation (right), for Pb+Pb Reaction at energy $\sqrt{s}$=2.76 TeV. Figure from [37].

to impact parameter. The center of mass rapidity, y_{CM}, fluctuates partly due to the large rapidity difference between projectile and target and partly due to the event-by-event CM fluctuations arising from the different participant numbers coming from the projectile and from the target. The azimuthal angle of the Reaction Plane, Ψ_{RP} will also be modified by the event-by-event fluctuations, which is taken into account in Ref. [38]. Thus the fluctuating collective flow is usually analyzed by:

$$\frac{d^3N}{dydp_td\phi} = \frac{1}{2\pi}\frac{d^2N}{dydp_t}\left[1 + 2v_1(y,p_t)\cos(\phi - \Psi_1^{EP}) + 2v_2(y,p_t)\cos(2(\phi - \Psi_2^{RP})) + \cdots\right] . \tag{3.3}$$

where ϕ and Ψ_n^{EP} are measured in the laboratory (collider) frame. Ψ_n^{EP} maximizes $v_n(y,p_t)$ in a rapidity range. For exactly central collisions this calculation is adequate since the Global Collective flow will not lead to azimuthal asymmetries, but for peripheral collisions the analysis is problematic since the flow patterns arising from the Global Collective flow and from fluctuations are mixed up. Similarly for spherical or cylindrical symmetry the separation is more subtle because it does not show up directly in the

azimuthal flow harmonics. The fluctuations in the transverse plane and Global Collective flow (background flow) were studied and separated in [39] in special model calculations.

Based on the final components of given types of symmetries arising from the initial states symmetries in peripheral heavy ion collisions, the Eq. (3.3) can be reformulated in order to make the splitting of the Global Collective flow from Fluctuations easier. By using the relation $\cos(\alpha - \beta) = \cos\alpha\cos\beta + \sin\alpha\sin\beta$, each harmonic expansion term can be written as:

$$v_n \cos[n(\phi - \Psi_n^{EP})] = v_n \cos(n\Psi_n^{EP}) \cos(n\phi) + v_n \sin(n\Psi_n^{EP}) \sin(n\phi) \ ,$$

here we define ${}^{c}v_n \equiv v_n \cos(n\Psi_n^{EP})$ and ${}^{s}v_n \equiv v_n \sin(n\Psi_n^{EP})$. We can introduce $\Phi_n^{EP} \equiv \Psi_n^{EP} - \Psi_{RP}$ and $\phi' \equiv \phi - \Psi_{RP}$, if the unique Reaction Plane Ψ_{RP} can be determined event-by-event experimentally as in [40]. Thus we have $\Psi_n^{EP} = \Phi_n^{EP} + \Psi_{RP}$ and $\phi - \Psi_n^{EP} = \phi' - \Phi_n^{EP}$ where ϕ' is the azimuth angle with respect to the Reaction Plane. By using these definitions the flow harmonic coefficients take the form:

$$v_n \cos[n(\phi - \Psi_n^{EP})] = v_n \cos[n(\phi' - \Phi_n^{EP})] = {}^{c}v'_n \cos(n\phi') + {}^{s}v'_n \sin(n\phi') \ , \qquad (3.4)$$

where ${}^{c}v'_n \equiv v_n \cos(n\Phi_n^{EP})$ and ${}^{s}v'_n \equiv v_n \sin(n\Phi_n^{EP})$. Thus we reformulated the harmonic expansion in terms of both sines and cosines in the Reaction Plane as reference plane with the new coefficients ${}^{c}v'_n = {}^{c}v'_n(\boldsymbol{y}, p_t)$ and ${}^{s}v'_n = {}^{s}v'_n(\boldsymbol{y}, p_t)$ where $\boldsymbol{y}$ is the rapidity variable $\boldsymbol{y} \equiv y - y_{CM}$. The parameters v_n, Ψ_n^{EP}, Ψ_{RP} and y_{CM} can be obtained from the measured data directly in experiments. Since the Global Collective flow is $\pm y$ symmetric in the configuration space, the $\sin(n\phi)$ terms should vanish (${}^{s}v'_n = 0$), or it may have some non-zero value arising from fluctuations only. Thus, these properties provide a possibility to separate the fluctuating and global flow components [41].

This form, Eq. (3.4) has the advantage that in peripheral collisions the Global Collective (not fluctuating) flow component, ${}^{c}v'_n$ is odd (even) functions of $\boldsymbol{y}$ for odd (even) harmonics. However this is not usually satisfied due to the fluctuations, thus

we have to construct the even (odd) combinations from the measured data. We can obtain the fluctuating component by subtracting the Global Collective component from the total flow harmonic term:

$$v_{n\,\frac{\text{even}}{\text{odd}}}^{\text{Coll.}} \cos[n(\phi - |Psi_n^{EP})] = \frac{1}{2}\,[\ {}^{c}v_n'(\boldsymbol{y}, p_t)\ \pm\ {}^{c}v_n'(-\boldsymbol{y}, p_t)]\cos(n\phi)\ , \tag{3.5}$$

$$v_{n\,\frac{\text{even}}{\text{odd}}}^{\text{Fluct.}} \cos[n(\phi - |Psi_n^{EP})] = \frac{1}{2}\,[\ {}^{c}v_n'(\boldsymbol{y}, p_t)\ \mp\ {}^{c}v_n'(-\boldsymbol{y}, p_t)]\cos(n\phi) + {}^{s}v_n'(\boldsymbol{y}, p_t)\sin(n\phi)\ . \tag{3.6}$$

If the fluctuations show the same symmetries in some events as the Global Collective Flow, this separation will provide a maximum magnitude for the Global Collective Flow component. On the other hand the Fluctuating component term should also have a maximum because the ${}^{s}v_n'$ term can not be affected by the Global Collective flow and it must have the same magnitude for sine and cosine components as well as for odd and even rapidity components. This separation may provide a better insight into the two flow patterns if the experimental results are evaluated this way [41]. Furthermore, this can also be used to help judge the theoretical model results as well as the theoretical assumptions regarding the initial states.

Chapter 4

Rotation and turbulent instability

Recent theoretical developments and experimental observation of high multipolarity fluctuations indicate that the QGP is a low viscosity fluid, which makes turbulent phenomena possible [42, 43, 44]. Usually the KHI will occur when there is velocity shear in one continuous fluid or when the velocity is different across the interface between two fluids. The QGP produced for high energy peripheral collisions can be treated as one fluid with different shear velocity, under favorable conditions the initial development of KHI is then observed in our high resolution and low numerical viscosity Fluid Dynamical model, see [42]. This instability may lead to a significant rotation and it can be characterized by the flow vorticity. Some other issues like what is the condition for KHI development, how it depends on quantities (i.e., the viscosity and the surface tension), how this rotation can be damped by the longitudinal and transverse expansion of the system are also studied in this chapter.

4.1 Flow vorticity

In fluid dynamics the vorticity is a field vector, which can describe the local rotating or spinning movement of some point. We can mark that point and observe the displacement of the surrounding particles. A two-dimensional flow has vorticity which is always perpendicular to the plane of the flow, and therefore it can be considered as a vector field.

Mathematically simple flows are usually considered as potential flows, whose velocity can be calculated from a potential $v = \nabla\phi$, thus the vorticity of potential flow is zero meaning that there is no vorticity in the potential flow. However the naturally occurring flows are mainly vortical. Classically the vorticity of a flow is defined to be the curl (rotation) of velocity field, and it is normally denoted by the symbol ω. In 3-dimensional space the vorticity is defined as:

$$\omega = \frac{1}{2}\nabla \times \boldsymbol{v} \ . \tag{4.1}$$

Here the factor 1/2 is introduced for symmetrization needed in our calculation in [6]. The vorticity is related to the flow's circulation, which is defined as the line integral of velocity over the curve C and can be calculated in terms of the vorticity by using Stokes' theorem:

$$\Gamma = \oint_C \boldsymbol{v} d\boldsymbol{l} = \int 2\boldsymbol{\omega} d\boldsymbol{S} \ , \tag{4.2}$$

where S is the closed surface element surrounded by the curve C.

In relativistic case the vorticity is defined as

$$\omega_{\mu\nu} = \frac{1}{2}(\partial_\nu u_\mu - \partial_\mu u_\nu) \ , \tag{4.3}$$

where $\partial_\nu = (\partial_0, \partial_x, \partial_y, \partial_z)$ and $u_\mu = \gamma(1, -v_x, -v_y, -v_z)$. In the reaction $[x, z]$ plane the vorticity is:

$$\omega_{y(Cl.)} = \frac{1}{2}(\partial_z v_x - \partial_x v_z) \ , \tag{4.4}$$

$$\omega_{y(Re.)} = \frac{1}{2}(\partial_z \gamma v_x - \partial_x \gamma v_z) \ , \tag{4.5}$$

where "Cl."denotes classical case and "Re." denotes relativistic case.

In our PICR Hydrodynamical model the fluid cells are in three dimensions and we

Average relativistic vorticity

		dx=0.585fm, $b/b_{max} = 0.5$		dx=0.4375fm, $b/b_{max} = 0.7$	
Timestep	Time (fm/c)	Relativistic	Classical	Relativistic	Classical
Reaction plane					
4	0.17	0.02415	0.05839	0.11846	0.14343
84	3.56	0.01677	0.01622	0.07937	0.04845
164	6.94	0.01295	0.00606	0.05116	0.01555
All layers					
4	0.17	0.07241	0.09442	0.19004	0.1971
84	3.56	0.05242	0.03086	0.10685	0.0538
164	6.94	0.0344	0.01185	0.05881	0.0159

Table 4.1: Averaged weighted relativistic vorticity calculated for the Reaction Plane (at $y = 0$) and for each [x-z] layer and averaged over all layers for Pb+Pb reactions at $\sqrt{s_{NN}} =$ 2.76TeV, reactions at different grid resolutions dx=dy=dz and impact parameters.

only calculate the vorticity in the reaction [x,z] plane in the y direction, more calculation details are shown in Appendix C. Since the system is expanding and it becomes highly nonhomogeneous, the number of cell with particles are increasing thus the energy per cell is decreasing, we weight the vorticity by the energy density, that is $\Omega_y = w(x, z)\omega_y$, where the average of weight $< w(x, z) >= 1$. Then the vorticity is calculated at LHC energy in Ref. [6] as well as at NICA and FAIR energy just above the threshold of transition to QGP in Ref. [1].

In Ref. [6] the vorticity is calculated for Pb + Pb collision at center of mass energy $\sqrt{s_{NN}} = 2.76$ TeV. The vorticity is 10 times larger (3 c/fm) than the one (0.2 c/fm) [44] raised from random fluctuations in transverse plane, since in the Reaction Plane the vorticity arises from the large initial angular momentum for peripheral collisions, while in the transverse plane it is caused only by random fluctuations.

For more peripheral collisions, i.e., impact parameter $b = 0.7\ b_{max}$, the initial condition is favoring more the KHI thus the average velocity is larger when compared with more central collision with impact parameter $b = 0.5\ b_{max}$. This effect can be seen apparently in table 4.1, with larger impact parameter and smaller cell size, the KHI is more obvious characterized by the larger vorticity.

The vorticity and circulation decreases rapidly due to the explosive expansion of

the system as shown in the figure series in paper [6], however the peak vorticity is 3 c/fm in favorable configurations with KHI development and is 1 c/fm for less favorable configurations at time 4 fm/c after the beginning of fluid dynamical expansion (Fig. 12 in paper [6]).

As discussed not only the predicted average vorticity is substantial but also the peak vorticity, thus it is possible to observe the consequences of this rotation and its sensitivity to turbulent configurations.

In Ref. [1] the vorticity is calculated the same way as in Ref. [6] but only for lower energies, in order to study the possibility of vorticity and circulation in dense plasma at lower temperatures. We analyze the Au + Au collisions at $\sqrt{s_{NN}} = 9.3$ GeV for NICA and U + U collisions at $\sqrt{s_{NN}} = 9.0$ GeV for FAIR. If the collision energy is not sufficient to achieve QGP formation, the larger hadronic pressure will lead to earlier and more rapid expansion thus the rotational energy will be reduced faster and converted into more explosive expansion. Although the magnitude is smaller than the one obtained for higher energy, the vorticity still remains significant.

4.2 Viscous potential flow analysis

The KHI will be affected by the surface energy and the viscosity. In fluid dynamics the onset of turbulence has less possibility to develop in more viscous fluids with large surface tension. Thus it is important to study how the KHI and rotation will be influenced by the surface energy and the viscosity.

Following the work done in Ref. [45], we assume an initial state where the shear is localized at the dividing plane between the top half and the bottom half of the fluids, see Fig. 3 in Ref. [5], the two parts are separated by an energetically motivated hypothetical surface, characterized with a phenomenological surface tension. The collective flow is considered as a "shear flow" since the top participant layers are moving nearly with projectile velocity while the bottom layers are moving with the target velocity. We allow

the fluid slip at the top and bottom boundaries and the dividing surface between them will be referenced as unconstrained slip-condition. Then the growth rate of the instability is computed as a function of phenomenological parameters characteristic for the QGP fluid: viscosity, surface tension, and flow layer thickness.

The viscosity can be estimated from the cell size in PICR method, where small viscosity corresponds to small cell size. The surface tension is neglected at early stage compared to the energy of the collective flow for RHIC and LHC energy collisions, which mainly hinders the early emission of low energy hadrons from the plasma, while it does not hinder the rotation. This is not the case when the KHI develops between two fluids (e.g. water/air or oil/air), where the large surface tension (e.g. between oil and air) can hinder the development of KHI. In our case the KHI is developing within one fluid (QGP), although there is no surface tension in the conventional sense, however, due to the large shear between the two fluid layers, the layer with the high shear may have extra energy, thus it can lead to an effective surface tension which can weaken the development of KHI.

In this idealized analytic model [5], the KHI is developing under similar conditions, as in numerical high resolution relativistic fluid dynamical calculations [42]. After some calculations we get the growth rate, σ, as function of the layer thickness l, the viscosity η and the surface tension γ. In heavy ion collisions, the matter will expand after the collision, thus in fact there is no external boundary (top and bottom) of the fluid, so we can assume $l \to \infty$, we get the equation:

$$\sigma_R = -\frac{k^2\eta}{\rho} \pm \sqrt{\frac{k^4\eta^2}{\rho^2} + \frac{k^2(U_t - U_b)^2}{4} - \frac{\gamma k^3}{2\rho}} \,. \tag{4.6}$$

Then we assume that the top and bottom layers have velocity difference $|U_t - U_b| = 0.8$ c. The effective mass density ρ of QGP and the wave number k are respectively $\rho = 0.6$ and $k = 0.6$ according to the estimation in [42]. After such assumption, we can obtain the growth rate dependence of the viscosity and the surface tension. As a result the

growth rate of KHI is influenced both by the viscosity and the effective surface energy. The growth rate decreases when the viscosity increases suggesting that the KHI grows weaker for a more viscous fluid, see Fig. 4,5 in Ref. [5].

As expected, larger surface tension or surface energy damps the growth of KHI, with bigger surface tension the KHI effect is less probable to appear. We also find a critical surface energy, $\gamma_{crit} \approx 5.3$ GeV/fm and interestingly this critical surface tension does not depend on the viscosity. At this critical point the growth rate is zero and becomes negative afterwards.

In order to have positive growth rate of KHI, the velocity difference $V = U_t - U_b$ between two layer should satisfy the condition $V^2 > \frac{2\gamma k}{\rho \coth(kl)}$. As investigated, the KHI will only occur when the velocity difference is larger than this critical velocity. The wave number of the fluids should satisfy

$$\frac{2\pi}{l_z} \leq k \leq \frac{2\pi}{\lambda_K}$$

, where l_z is the beam directed longitudinal length of the flow and λ_K is the Kolmogorov length scale [42]. For more peripheral collisions the instability is able to grow faster and the system tends to be unstable.

If we do not assume $l \to \infty$, we can get the growth rate as function of the thickness as well as viscosity and surface tension. Unlike the classical gravitational water waves where the wave formation and wave speed depends strongly on the depth of the water, the role of the layer thickness does not influence much of the growth rate of KHI in heavy ion collisions, because there is no solid boundary and the system expands in all directions. Thus the large or infinite layer thickness is more relevant in this model, even if the initial layer thickness is finite and usually smaller than the longitudinal size of the initial state.

This paper confirms that the dependence of the growth rate on the viscosity reflects the usual tendency that instability and turbulence increases with smaller viscosity.

4.3 Rotation in an exact hydrodynamical model

In heavy ion collisions the rotation can be neglected if we only consider head on collisions. For more peripheral collisions this effect should be considered an the exploding system which have a big non-vanishing initial angular momentum presented in the initial conditions. Rotating fluids are numerically investigated in relativistic hydrodynamics [5, 6, 31, 37, 42] and exact analytic solutions of relativistic and nonrelativistic hydrodynamics are also studied [46, 47]. By recapitulating the quantities from Ref. [47], we use the fluid dynamical calculations to test a new family of exact rotating solutions, which may provide a more fundamental insight to the interaction between the rotation and expansion of the system in Ref. [2].

We consider the the solution of the conventional form of non-relativistic hydrodynamics equations:

$$n\, m\, (\partial_t + \boldsymbol{v}\cdot\nabla)\boldsymbol{v} = -\nabla p \ , \tag{4.7}$$

where the pressure is $p = nT$. The energy density is a function of pressure with the factor κ only depend on temperature $\epsilon = \kappa(T)p$. If we assume $\kappa(T)$ is constant, which means it is independent of temperature, this corresponds to the case of 1A in Ref. [47]. In this case the temperature is $T = T_0 \left(\frac{V_0}{V}\right)^{1/\kappa} \mathcal{T}(s)$, where $\mathcal{T}(s)$ is an arbitrary normalized positive function. The energy density is $n = n_0 \frac{V_0}{V}\nu(s)$ and $\nu(s) = \frac{1}{\mathcal{T}(s)} e^{-\frac{1}{2}\int_0^s \frac{du}{\mathcal{T}(u)}}$, where the spatial scale s is chosen in a cylindrical coordinates in length dimension (r_ρ, r_ϕ, r_y) instead of x, y, z, then we have so called "out, side, long" directions with the variables:

$$s_\rho = r_\rho^2/R^2, \quad s_\varphi = r_\varphi^2/S^2 \quad s_y = r_y^2/Y^2 \ ,$$

in this coordinate system the velocity is $\boldsymbol{v} = v_\rho \boldsymbol{e}_\rho - v_\varphi \boldsymbol{e}_\varphi + v_y \boldsymbol{e}_y = \frac{\dot{R}}{R} r_\rho \boldsymbol{e}_\rho - \omega r_\rho \boldsymbol{e}_\varphi + \frac{\dot{Y}}{Y} r_y \boldsymbol{e}_y$.

By solving the Euler's equation, Eq. (4.7), with the help of energy conservation laws, we estimate the rate of slowing down of the rotation due to the longitudinal and trans-

verse expansion of the system. In fact in this work we neglected the z directed elongation in the Reaction Plane, that the x and z coordinates are considered as azimuthally symmetric and can be characterized by the radial component R, thus the energy contains the radial and longitudinal expansion energies as well as the rotational one. The calculation of the baryon density, the momentum inertia and the kinetic energy are shown in Appendix D. The second order differential equation can be solved numerically by the Runge Kutta method. The initial state parameters of the model are extracted from our high resolution (small viscosity) PICR model calculation [42] of a Pb+Pb collisions at $\sqrt{s_{NN}} = 2.76$ A TeV with impact parameter $b = 0.7 b_{max}$, where the initial angular momentum of the system is $L_y = -1.05 \times 10^4 \hbar$.

It turns out that the exact solution is only able to describe the monotonic expansion, the rotation is decreasing steadily, unlike in our PICR fluid dynamical model where the rotation first increases due to the initial angular energy from the initial state shear and then starts to decrease. Thus in this exact model we start from a higher initial angular velocity. As expected the total energy of the rotating system is conserved, the kinetic energy of expansion is increasing while the rotation and internal energy are decreasing, see Fig. 1 in Ref. [2].

The expansion velocity is increasing in the radial R direction and axial Y direction, see Fig. 2 in Ref. [2]. The radial expansion velocity increases by 10 percent and increases faster compared to the expansion in the direction of the axis of rotation (y), partly due to the centrifugal acceleration of the rotation and partly due to the initially smaller transverse size. In fact this exact fluid model overestimates the radial expansion due to the lack of dissipation, thus the system is already 16 fm at 8 fm/c which means the Freeze out happens earlier than this time.

The exact model describes a system with a single uniform angular velocity and provides an estimate of the rate of decrease of angular speed and rotational energy due to the expansion in an explosively expanding system. This indicates that rotation effects can be observed in case of rapid freeze out and hadronization. The uniform flow can

develop from the initial shear flow at different times depending on the impact parameter, the system size, the beam energy, and the transport properties. It is important to know the parameters reached at some definite time in a collision which can enable us to obtain the material parameters and the equilibration dynamics. This exact model provides us a simple and straightforward tool to give a precise estimate about the time moment when the rotation is equilibrated and what are the parameters of the matter at that moment.

Chapter 5

Methods to detect rotation

The rotation lead by the KHI can be detected by three methods. The first one is the directed flow however it is weak at higher enengy collisions such as at LHC and RHIC energy. The other methods are the Λ polarization observation and the two particle correlation function of the system.

5.1 Thermal polarization of Λ particles

The polarization is one of the consequences of rotation and local vorticity induced by the shear flow of the expanding system. In Ref. [48] a polarization formula is obtained by assuming weakly interacting particles described by the Cooper-Frye method. With the assumption of local spin degrees of freedom and its equipartition with rotation, the polarization turns out to be proportional to the vorticity of the inverse temperature 4-velocity field:

$$\beta_\mu(x) = \frac{u_\mu(x)}{T} \ . \tag{5.1}$$

LHC (Pb+Pb @ 1.38+1.38 A·TeV)				RHIC (Au+Au @ 100+100 A·GeV)			
ncyc	t (fm/c)	$\langle T \rangle$ (MeV)	$\langle \Omega_{zx} \rangle$ $(1/\hbar)$	ncyc	t (fm/c)	$\langle T \rangle$ (MeV)	$\langle \Omega_{zx} \rangle$ $(1/\hbar)$
88	3.72	379	0.0301	28	1.19	285	0.0976
132	5.59	299	0.0237	44	1.86	261	0.0915
180	7.62	246	0.0172	60	2.54	237	0.0851
268	11.34	201	0.0077	88	3.72	204	0.0664
360	15.24	186	0.0027	112	4.74	183	0.0453

Table 5.1: Averaged weighted relativistic thermal vorticity calculated for the Reaction Plane for LHC and RHIC energies.

Similarly to the normal vorticity calculated in Eq. (4.2), the thermal vorticity is defined as:

$$\varpi^{\mu\nu} = \frac{1}{2}(\partial^{\nu}\beta^{\mu} - \partial^{\mu}\beta^{\nu}) \ . \tag{5.2}$$

We calculate the thermal vorticity in our hydrodynamical model [4]. As discussed before, the vorticity is larger for higher energies thus we assume that the thermal vorticity is also larger for higher energy collisions. However this is not true, to be more precise we studied the thermal vorticity for both LHC and RHIC energies, see Fig. 5 in Ref. [9]. We introduced the weighting factor the same way as done for normal vorticity since at late stages the energy density or the net baryon density tend to zero in the middle, which domain then should not be taken into account.

The average energy weighted thermal vorticity is shown in table 5.1. As shown in the table the average thermal vorticity is smaller for LHC energy compared to RHIC. At ultra-relativistic energies the velocities are approaching the speed of light and the initial state velocity distributions are essentially identical. At the same time the initial energy density is much higher at LHC, thus the angular momentum and the initial temperature also. As a consequence the thermal vorticity is smaller since the temperature is in the denominator. The following expansion is more rapid at the higher energies, thus with faster expansion the local vorticity decreases also faster as shown in Ref. [6], just as the average temperature shown in Ref. [7]. On the other hand the final, freeze out

temperatures should not be too different, although at higher expansion speed the freeze out temperature is expected to be higher also.

The space integrated mean polarization vector can be calculated for relativistic heavy ion collisions by assuming a 3-dimensional space like freeze out hypersurface (Σ), based on the assumption of local thermodynamical equilibrium at freeze out, we have:

$$\Pi_\mu(p) = \hbar\epsilon_{\mu\rho\sigma\tau}\,\frac{p^\tau}{8m}\frac{\int \mathrm{d}\Sigma_\lambda p^\lambda\, n_F(1-n_F)\partial^\rho\beta^\sigma}{\int \mathrm{d}\Sigma_\lambda p^\lambda\, n_F}\ , \tag{5.3}$$

where n_F is the Fermi-Jüttner distribution of Λ. According to the Copper-Frye description we have $d\sigma_\lambda p^\lambda \to dVp^0$ for constant time freeze out at a given stage of fluid dynamic expansion. Also due to overall parity invariance, the polarization vector can be simplified to

$$\mathbf{\Pi}(p) = \frac{\hbar\varepsilon}{8m}\frac{\int \mathrm{d}V\, n_F\ (\nabla\times\boldsymbol{\beta})}{\int \mathrm{d}V\, n_F}\ . \tag{5.4}$$

As shown in this equation, the polarization is essentially a thermo-mechanical effect, namely calculated from the thermal vorticity, thus one important distinctive features is that the polarization vector has the same direction for both particles and antiparticles. Due to this definition the final observed polarization is less sensitive on beam energy than the final (speed) vorticity or the temperature, because in the thermal vorticity the changes of the temperature and vorticity balance each other, see Fig. 6 in Ref. [9]. The polarization or the thermal vorticity change are only second order effects, and these depend on the relative rates of decrease of the vorticity and of the temperature. Therefore the final polarizations and thermal vorticities are not so different as the angular momenta or the initial temperatures.

The polarization of Λ is investigated since its dominant decay mode is $\Lambda \to p\pi^-$ where the proton p is emitted in the polarization direction. However for lower energy collision, the multiplicity of Λ particles is small thus we need to choose some other high multiplicity particles to measure the polarization.

Here for LHC and RHIC energies we can study the Λ particle polarization in its local rest frame $\mathbf{\Pi}_0$. As we can see in [4] the polarization increases with the transverse momentum p_T and it is sensitive to flow properties and asymmetries. Also the polarization is largest at the Reaction Plane, thus the utmost thing is to identify the Reaction Plane. Without this the polarization is not possible to observe. One earlier measurement at RHIC has the conclusion that the measured polarization is zero since they have averaged the polarization overall azimuthal angles.

The thermal polarization may reach sizable and detectable values which is several percent when the momentum is in several GeV magnitude. On the other hand if the source of the expanding participant system does not have significant rotation, then we can not measure the thermal polarization. Thus it provides a way to detect the rotation effect for peripheral collisions with large initial angular momentum.

5.2 Differential Hanbury Brown and Twiss method

The two particle correlation method is originally used to detect the size of distant stars [49]. It can also be used in heavy ion physics to determine the size as well as its ellipsoidal tilted shape of the colliding system. Ref. [50] analyzed the effect of flow on two particle correlations and the HBT radius should have a minimum at the phase-transition threshold [51]. Due to the expansion of collective flow, the size estimated by the method may be modified. In Ref. [52] the two particle correlation method is used to study the rotation for few source models, such as for two steady/moving sources, four moving sources. We start from the pion correlation function which is defined as:

$$C(p_1, p_2) = \frac{P_2(p_1, p_2)}{P_1(p_1)P_2(p_2)} \ , \tag{5.5}$$

where p_1 and p_2 represent the 4-momenta, P_1 is the inclusive one particle distribution while P_2 is the inclusive two particle distribution. Assume that two particles are emitted from space time points x_1 and x_2, the particle distribution can be calculated

as $P_2(p_1,p_2) = \int d^4x_1 d^4x_2 S(x_1,p_1)S(x_2,p_2)|\psi_{12}|^2$. Here $S(x,p)$ is the source function and we make Jüttner approximation for it in our calculation. The wave function is $\psi_{12} = \frac{1}{\sqrt{2}}(e^{ip_1\cdot x_1+ip_2\cdot x_2} + e^{ip_1\cdot x_2+ip_2\cdot x_1})$.

By introducing the center of mass momentum $k = \frac{1}{2}(p_1+p_2)$ and the relative momenta $q = p_1 - p_2$, the momentum can be expressed as $p_1 = k + q/2$ and $p_2 = k - q/2$. From the mass-shell condition we get $q^0 = \boldsymbol{kq}/k^0$. Thus the two particle distribution takes the form:

$$\begin{aligned} P_2(p_1,p_2) &= \int d^4x_1\, d^4x_2\, S(x_1,k+q/2)\, S(x_2,k-q/2) \\ &\times \left[1 + \frac{1}{2}\left(e^{iq\cdot(x_1-x_2)} + e^{-iq\cdot(x_1-x_2)}\right)\right] . \end{aligned} \tag{5.6}$$

Then the correlation function is:

$$C(k,q) = 1 + \frac{R(k,q)}{\left|\int d^4x\, S(x,k)\right|^2} , \tag{5.7}$$

where $R(k,q) = \int d^4x_1\, d^4x_2\, \cos[q(x_1-x_2)] S(x_1,k+q/2)\, S(x_2,k-q/2)$ and it can be calculated as $R(k,q) = \mathrm{Re}\,[J(k,q)\, J(k,-q)]$ where the function $J(k,q) = \int d^4x\ S(x,k+q/2)\, \exp(iqx)$. By using the local Jütterner distribution we have

$$\begin{aligned} R(k,q) = \int & d^4x_1 d^4x_2\, S(x_1,k) S(x_2,k) \cos[q(x_1-x_2)] \times \\ & \exp\left[-\frac{q}{2}\cdot\left(\frac{u(x_1)}{T(x_1)} - \frac{u(x_2)}{T(x_2)}\right)\right] , \end{aligned} \tag{5.8}$$

and the J function is

$$J(k,q) = \int d^4x\ S(x,k)\, \exp\left[-\frac{q\cdot u(x)}{2T(x)}\right]\, \exp(iqx) . \tag{5.9}$$

This can be used to calculate the systems with one-, two- and four sources. For example for the four moving sources shown in the l.h.s of Fig. 5.1. On the r.h.s. of Fig. 5.1 the size of the sources represents the possibility of reaching the detectors located on the k_+

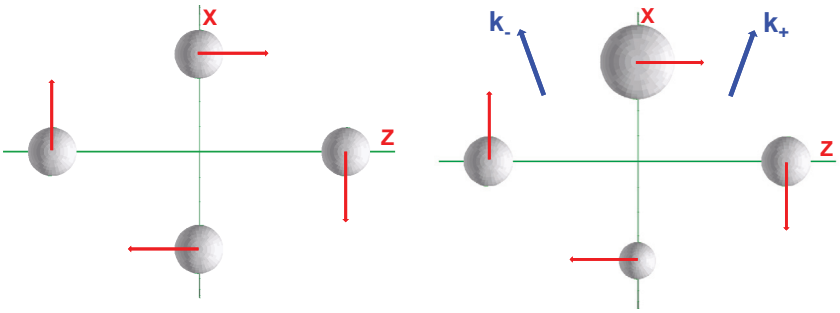

Figure 5.1: (Color online) Four moving sources in the Reaction Plane. The blue lines represent the detectors. Figure from [52].

and k_- directions. The pions emitted from the sources near the detectors have larger possibility to reach them. This effects can be characterized by the weights.

The $\boldsymbol{k}$-dependent coordinate system is introduced to classify the direction of $\boldsymbol{q}$ in order to detect the correlation function in the Reaction Plane (which means the rotation axis is y directed, we define

$$\hat{\boldsymbol{k}}_\pm = (a, 0, \pm b)\mathrm{fm}^{-1},\ k_x = a|\boldsymbol{k}|,\ k_z = \pm b|\boldsymbol{k}|, \tag{5.10}$$

where $a^2 + b^2 = 1$, see r.h.s. of Fig. 5.1. The source has a given "out-direction" of momentum k which can be measured by two detectors on both sides of the emitting sources with momentum k_+ and k_-. In the mean time the relative momentum vector, $\boldsymbol{q}$, can be measured in the directions

$$\begin{aligned}
\hat{\boldsymbol{q}}_{out} &= (a, 0, \pm b),\ q_x = a|\boldsymbol{q}|,\ q_z = \pm b|\boldsymbol{q}|\ , \\
\hat{\boldsymbol{q}}_{side} &= (0, 1, 0), \quad q_y = |\boldsymbol{q}|\ , \\
\hat{\boldsymbol{q}}_{long} &= (\mp b, 0, a), \quad q_x = \mp b|\boldsymbol{q}|,\ q_z = a|\boldsymbol{q}|\ .
\end{aligned} \tag{5.11}$$

Thus the difference of the forward and backward shifted correlation function of the out component can be calculated:

$$\Delta C(k_\pm, q_{out}) \equiv C(k_+, q_{out}) - C(k_-, q_{out})\ . \tag{5.12}$$

This is called the Differential Correlation function (DCF) or Differential HBT (DHBT). If the sources are static, spherically or cylindrically symmetric, or if the sources only have the radial velocities, the DCF will vanish. But if the local velocities of the sources have a "side" component or in other words if the system is rotating, the DCF is not zero and increases with increasing rotational velocity.

This DHBT can be calculated for fluid dynamic cells where each cell can be considered as emitting source [3], more detailed calculation of correlation function are shown for two fluid cells, eight fluid cells and all the fluid cells in Appendix E. Here we show the calculation in an simplified way, we first calculate the correlation function by using:

$$\begin{aligned} \int d^4x\, S(x,k) &= \sum_s \int_s d^3x_s\, dt_s\, S(x_s,k) \\ &= (2\pi R^2)^{3/2} \sum_s \frac{\gamma_s n_s(x)\,(k_\mu\, \hat{\sigma}_s^\mu)}{C_s}\, \exp\left[-\frac{k\cdot u_s}{T_s}\right] , \\ J(k,q) &= \sum_s e^{-\frac{q}{2}\cdot\frac{u_s}{T_s}}\, e^{iqx_s} \int_s d^4x\; S_s(x,k)\, e^{iqx} , \end{aligned} \tag{5.13}$$

where Θ_s is the path length of the time integral from the space time point of the source s. The weight of each cell as emitting source is $w_s = (\gamma_s k_0 + \boldsymbol{k}\boldsymbol{u}_s)\exp(-\Theta^2 q_0^2/2)$, see more details in Appendix E. It determines which cells contribute more and which cells contribute less to the integrals. We reassign the summation in Eqs. (5.14) from single cell to cell pairs, which means the summation $s = \{i,j,k\}$ will correspond to a pair of cells: the cell $\{i,j,k\}$ and its reflected pair across the c.m. point at the same time at $\{i^*,j^*,k^*\}$. In order to simplify the calculation we introduce the following definitions:

$$\begin{aligned} Q_c &= \left(2\pi R^2\right)^{3/2} \exp\left[-\frac{R^2q^2}{2}\right] , \\ P_s &= \frac{\gamma_s n_s}{C_s} \exp\left[-\frac{k_0\, u_s^0}{T_s}\right] , \\ Q_s^{(q)} &= \exp\left[-\frac{q_0\, u_s^0}{2T_s}\right] , \\ w_s &= (k_\mu\, \hat{\sigma}_s^\mu)\; \exp\left[-\frac{\Theta_s^2}{2} q_0^2\right] . \end{aligned} \tag{5.14}$$

Thus the Eqs. (5.14) become:

$$\int d^4xS(x,k) = \left(2\pi R^2\right)^{3/2} \sum_s P_s \left[w_s \exp\left(\frac{\boldsymbol{k}\boldsymbol{u}_s}{T_s}\right) + w_s^* \exp\left(\frac{\boldsymbol{k}\boldsymbol{u}_s^*}{T_s}\right)\right]$$
$$J(k,q) = Q_c \sum_s P_s \left[Q_s^{(q)} w_s \exp\left[\left(\boldsymbol{k}+\frac{\boldsymbol{q}}{2}\right)\frac{\boldsymbol{u}_s}{T_s}\right] e^{i\boldsymbol{q}\boldsymbol{x}_s} \right. \tag{5.15}$$
$$\left. + Q_s^{(q)} w_s^* \exp\left[\left(\boldsymbol{k}+\frac{\boldsymbol{q}}{2}\right)\frac{\boldsymbol{u}_s^*}{T_s}\right] e^{i\boldsymbol{q}\boldsymbol{x}_s^*}\right] .$$

The standard correlation function for an initial time ($t = 0.17$ fm/c) and for the final, FO time ($t = 3.56$ fm/c) is shown in Fig. 5.2 for $\boldsymbol{k}_+$, $\boldsymbol{q}_+$ direction. The k dependence of the correlation function is negligible at early stage and it becomes significant at later time. The width of the correlation function is narrower in q at later time primarily due to the rapid expansion of the system.

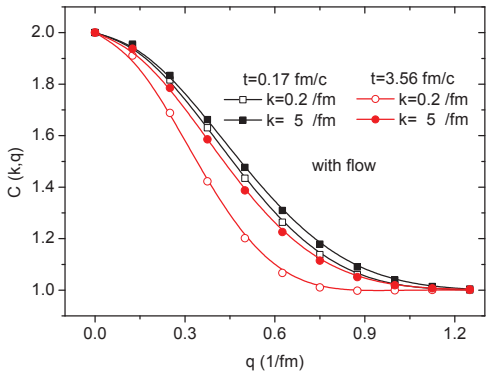

Figure 5.2: (color online) The correlation function in the $\boldsymbol{k}_+$ direction from a 3+1D fluid dynamical model at the initial and final times.

However the standard correlation is not only influenced by the emitting source velocity distribution but also by its shape. In theoretical models we can switch off the rotation component of the flow and analyze how the rotation influences the correlation function. We can rotate the original K frame by α angle and get the K' frame with axes x' and z', the momentum in K' frame is

$$\boldsymbol{k}'(\alpha) = \left\{ \begin{array}{c} k_{x'} \\ k_{z'} \end{array} \right\} = \left\{ \begin{array}{c} k_x \cos\alpha - k_z \sin\alpha \\ k_z \cos\alpha + k_x \sin\alpha \end{array} \right\} . \tag{5.16}$$

If the system is symmetric around the x' axis and if there are no flow, the DCF $\Delta C_\alpha(\boldsymbol{k}', \boldsymbol{q}') = 0$. Thus we first use DCF to find the symmetric axis of the emitting sources. In our calculation α is 11 degrees for Pb Pb collisions at LHC energy, see Fig. 4 in Ref. [3]. Then we can calculate the DCF in the K' frame which is deflected by α angle for the configurations with and without rotation. In this case the effects contributed to the DCF by the emitting source shape is eliminated, thus only the original, rotating fluid sources contribute to DCF. As expect the DCF is vanishing or minimal for the rotationless configuration. For rotational configuration the amplitude of the DCF doubles for the higher energy (higher angular momentum) collisions, Fig. 5 in Ref. [3]. Thus this provides an excellent method to detect the rotation of the system. However in experiment the rotationless configuration cannot be easily generated from experimental data. Thus methods like global flow tensor analysis and azimuthal HBT analysis [53] can provide an estimate for finding the deflection angle.

Chapter 6

Conclusion and outlook

In this thesis we have studied Kelvin Helmhotlz Instability induced by the large initial angular momentum for peripheral heavy ion collisions in the fluid dynamic model. This KHI will lead the turbulence and rotation effects. We first test how the KHI can be influenced by the normal parameters characterizing fluids such as the viscosity and the surface tension. Especially the viscosity is a key factor since the turbulence and the KHI occur only in case of low viscosity. Then we proposed an exact hydrodynamic model which provides a way to study the rotation and expansion analytically.

There are several methods to detect the rotation. The directed flow measurement is difficult due to its decreasing amplitude at increasing beam energies. As we know the flow vorticity is one direct phenomena induced by the rotation of fluid and this is studied in detail for higher collision energies and also for lower energy, which is just near the threshold of transition to QGP. Similarly with the vorticity we introduced the thermal voticity which can be used to calculate the polarization of particles. This is one method to detect the rotation of the expanding system. The observation of polarization would indicate the rotation of the system. Another method is the DHBT method, the differential correlation function should not be zero if the system has a rotating velocity, since if the system is symmetric and if there is no rotating velocity, the correlation function should be zero. We can have a better understanding of the Quark Gluon

Plasma by using these newly developed methods. The DHBT method has some other applications such as it can be used to study the rotation of binary stars in astrophysics, this work is in progress.

The significance of the achievements reported in the thesis and their evaluation

This thesis focused on studying a typical feature of the collective flow, namely the rotation of the flow, and the methods to detect the rotation in experiments. In this thesis we succeed in developing two methods to detect rotation, the polarization and the DHBT method.

The polarization is a consequence of rotation and vorticity arising from shear flow. It is different from the polarization arising from the magnetic field. This is called the thermal polarization and it has the same direction for both particles and antiparticles. The DHBT method is sensitive to the rotation of the expanding system. If the system is not rotating, then the Differential Correlation Function should be zero. It can correctly detect the rotation when we separate the correlation function caused by the rotation and by the source shape.

However, for these two methods, it is quite important to determine the Reaction Plane and the c.m. geometry, otherwise the effects may be eliminated by the integration over all directions.

These results are significant because they provide a substantially strong signal of rotation and turbulent instability like the KHI. The applicability of these new signals is presented in a convincing and transparent way, so we are confident that this will lead to experimental detection and quantitative measurements of these effects soon.

Bibliography

[1] L.P. Csernai, D.J. Wang, M. Bleicher and H. Stöcker, Phys. Rev. C **90**, 021904 (R) (2014). 3, 4, 29, 30

[2] L.P. Csernai, D.J. Wang and T. Csörgő, Phys. Rev. C **90**, 024901 (2014). 3, 4, 33, 34

[3] L.P. Csernai, V. Velle and D.J. Wang, Phys. Rev. C **89**, 034916 (2014). 3, 4, 43, 45

[4] F. Becattini, L.P. Csernai and D.J. Wang, Phys. Rev. C **88**, 034905 (2013). 3, 4, 38, 40

[5] D.J. Wang, Z. Néda and L.P. Csernai, Phys. Rev. C **87**, 024908 (2013). 3, 4, 30, 31, 32, 33

[6] L.P. Csernai, V.K. Magas and D.J. Wang, Phys. Rev. C 87, 034906 (2013). 3, 4, 28, 29, 30, 33, 38

[7] D.J. Wang, L.P. Csernai, D. Strottman, Cs. Anderlik, Y. Cheng, D.M. Zhou, Y.L. Yan, X. Cai and B.H. Sa, Eur. Phys. J. A **48**, 168 (2012). 3, 19, 21, 38

[8] L.P. Csernai, S. Velle and D.J. Wang, Nucl. Phys. A (2014), DOI: 10.1016/j.nuclphysa.2014.08.028. 3

[9] L.P. Csernai and D.J. Wang, EPJ Web of Conferences **71**, 00029 (2014), DOI: 10.1051/epjconf/20147100029. 3, 38, 39

[10] L.P. Csernai, F. Becattini and D.J. Wang, Journal of Physics: Conference Series **509**, 012054 (2014), DOI: 10.1088/1742-6596/509/1/012054. 3

[11] L.P. Csernai, A.M. Skålvik, D.J. Wang, D. Strottman, C. Anderlik, Y. Cheng, Y.L. Yan and B.H. Sa, Cent. Eur. J. Phys. **10**, 1271-1273 (2012). 3

[12] L.P. Csernai, A.M. Skålvik, D.J. Wang, V.K. Magas, H. Stöcker, D.D. Strottman, Y. Cheng and Y.L. Yan, Acta Phys. Polonica B **43**, 803 (2012). 3

[13] Introduction to Relativistic Heavy Ion Collisions, L.P. Csernai, John Wiley and Sons, Chichester, 1994, ISBN-471-93420-8. 7, 18

[14] V.K. Magas, L.P. Csernai and D.D. Strottman, Phys. Rev. C **64**, 014901 (2001); Nucl. Phys. A **712**, 167 (2002). 15, 23

[15] F. Cooper and G. Frye, Phys. Rev. D **10**, 186 (1974). 17

[16] L.P. Csernai, Zh. Eksp. Teor. Fiz. **92**, 379 (1987); Sov. JETP **65**, 213 (1987). 17

[17] K.A. Bugaev, Nucl. Phys. A **606**, 559 (1996). 18

[18] Cs. Anderlik, L.P. Csernai, F. Grassi, Y. Hama, T. Kodama, Zs. Lázár and H. Stöcker, Heavy Ion Phys. **9**, 193 (1999). 18

[19] K. Tamošiūnas and L.P. Csernai, Eur. Phys. J. A **20**, 269 (2004). 18

[20] M. Stephanov, K. Rajagopal and E. Shuryak, Phys. Rev. Lett. **81**, 4816 (1998). 19

[21] M. Stephanov, K. Rajagopal and E. Shuryak, Phys. Rev. D **60**, 114028 (1999). 19

[22] M.A. Stephanov, Phys. Rev. Lett. **102**, 032301 (2009). 19

[23] Y. Zhou, S.S. Shi, K. Xiao, K.J. Wu and F. Liu, Phys. Rev. C **82**, 014905 (2010). 19

[24] C. Nonaka and S.A. Bass, Phys. Rev. C **75**, 014902 (2007). 19

[25] C. Nonaka, M. Asakawa and S.A. Bass, J. Phys. G **35**, 104099 (2008). 19

[26] C. Nonaka, M. Asakawa, S.A. Bass and B. Muller, Nucl. Phys. A **830**, 291c (2009). 19

[27] L.P. Csernai, G. Mocanu and Z. Néda, Phys. Rev. C **85**, 068201 (2012). 19

[28] P. Huovinen and P. Petreczky, J. Phys. G: **38**, 124103 (2011). 20

[29] H. Niemi, G.S. Denicol, P. Huovinen, E. Molnar and D.H. Rischke, Phys. Rev. C **86**, 014909 (2012). 20

[30] P.K. Kovtun, D.T. Son and A.O. Starinets, Phys. Rev. Lett. **94**, 111601 (2005). 20

[31] L.P. Csernai, J.I. Kapusta and L.D. McLerran, Phys. Rev. Lett. **97**, 152303 (2006). 21, 33

[32] T. Schafer and D. Teaney, Rept. Prog. Phys. **72**, 126001 (2009). 21

[33] P.C. Hohenberg and B.I. Halperin, Rev. Mod. Phys. **49**, 435 (1977). 21

[34] L.P. Csernai and J.I. Kapusta, Phys. Rev. Lett. **69**, 737 (1992); Phys. Rev. D **46**, 1379 (1992). 21

[35] Ben-Hao Sa, Dai-Mei Zhou, Yu-Liang Yan, Xiao-Mei Li, Sheng-Qin Feng, Bao-Guo Dong and Xu Cai, Comp. Phys. Commun. **183**, 333 (2012). 21

[36] J. Cleymans, H. Oeschler, K. Redlich and S. Wheaton, Phys. Rev. C **73**, 034905 (2006). 21

[37] L.P. Csernai, V.K. Magas, H. Stöcker and D.D. Strottman, Phys. Rev. C **84**, 024914 (2011). 23, 24, 33

[38] Abeleev B et al, (ALICE Collaboration), Phys. Rev. Lett **111**, 232302 (2013). 24

[39] S. Floerchinger and U.A. Wiedemann, Phys. Rev. C **89**, 034914(2013) 25

[40] L.P. Csernai, G. Eyyubova and V.K. Magas, Phys. Rev. C **86**, 024912 (2012). 25

[41] L.P. Csernai and H. Stöcker, J. Phys. G in press, arXiv:1406.1153 (2014). 25, 26

[42] L.P. Csernai, D.D. Strottman and C. Anderlik, Phys. Rev. C **85**, 054901 (2012). 27, 31, 32, 33, 34

[43] A. Bonasera, Nuovo Cimento A **109**, 1405 (1996). 27

[44] S. Floerchinger and U.A. Wiedemann, Journal of High Energy Physics, doi:10.1007/JHEP 11, 100 (2011); J. Phys. G: Nucl. Part. Phys. 38, 124171 (2011). 27, 29

[45] T. Funada and D.D. Joseph, J. Fluid. Mech. **445**, 263-283 (2001). 30

[46] M.I. Nagy, Phys. Rev. C **83**, 054901 (2011). 33

[47] T. Csörgő and M.I. Nagy, Phys. Rev. C **89**, 044901 (2014). 33, 67, 68

[48] F. Becattini, V. Chandra, L. Del Zanna and E. Grossi, Annals of Physics **338**, 32-49 (2013). 37

[49] R. Hanbury Brown and R.Q. Twiss, Phil. Mag. **45**, 663 (1954); Nature **178**, 1046 (1956). 40

[50] Yu.M. Sinyukov, Nucl. Phys. A **498**, 151c (1989). 40

[51] Qingfeng Li, J. Steinheimer, H. Petersen, M. Bleicher and H. Stöcker, Phys. Lett. B **674**, 111 (2009); Qingfeng Li, M. Bleicher and H. Stöcker, Phys. Lett. B **659**, 525 (2008); Qingfeng Li, M. Bleicher, Xianglei Zhu and H. Stöecker, J. Phys. G **33**, 537 (2007). 40

[52] L.P. Csernai, V. Velle, arXiv:1305.0385. 40, 42, 79, 80

[53] M.A. Lisa, N.N. Ajitanand, J.M. Alexander, et al., Phys. Lett. B **496**, 1 (2000); M.A. Lisa, U. Heinz and U.A. Wiedemann, Phys. Lett. B **489**, 287 (2000); E. Mount,

G. Graef, M. Mitrovski, M. Bleicher and M.A. Lisa, Phys. Rev. C **84**, 014908 (2011); G. Graef, M. Bleicher and M. Lisa, Phys. Rev. C **89**, 014903 (2014). 45

[54] Sz. Horvát, V.K. Magas, D.D. Strottman and L.P. Csernai, Phys. Lett. B **692**, 277 (2010). 58

[55] M. Abramowitz and I.A. Stegun: *Handbook of mathematical functions* (Dover, New York, 1965), 6.5.2; I.S. Gradstein and I.M. Ryzhik: *Table of Integrals ...*, (Academic Press, 1994), 3.321/2., 3.361/1., 3.381/1., 8.250/1., 8.251/1., 8.350/1., 8.354/1. 69

[56] E. Molnár, L.P. Csernai, V.K. Magas, Zs.I. Lázár, A. Nyíri and K. Tamosiunas, J. Phys. G **34**, 1901 (2007). 80

[57] E. Molnár, L.P. Csernai, V.K. Magas, A. Nyiri and K. Tamosiunas, Phys. Rev. C **74**, 024907 (2006). 80

Appendix A

The CFD cell structure

In computational fluid dynamics (CFD) the spatial space is divided into many fluid cells. These fluid cells are spatially cubic and have the same cell size, d, in all spatial directions. The x, y, z axes situate at the edge lines of the first row cells in 3 directions, thus they are parallel to all the edges of the cells. The centers of the first row cells are at a distance $\frac{1}{2}d$ to the 3 axes.

It is sufficient to describe the cells only at positive y coordinate, since we have a initial state which is symmetric on negative and positive y direction with respect to the reaction $[x, z]$ plane. This means the negative y side cells are just the mirror image of the positive side ones. Thus the cells with negative y values are not calculated and stored in the code.

By labeling each cell center by the indexes i, j, k for x, y, z axes, the coordinate of the cell with index i, j, k is defined as:

$$\boldsymbol{x}_{ijk} = \left((i - i_{mid} - \frac{1}{2})d,\ (j - \frac{1}{2})d,\ (k - k_{mid} - \frac{1}{2})d \right), \tag{A.1}$$

where

$$\begin{aligned} i &= i_{min}, i_{min}{+}1,\ i_{min}{+}2, \ldots\ i_{max}\ , \\ j &= 1,\ 2,\ 3, \ldots\ j_{max}\ , \\ k &= k_{min},\ k_{min}{+}1,\ k_{min}{+}2, \ldots\ k_{max}\ . \end{aligned}$$

Here we always choose the values $i_{min} > 0$ and $k_{min} > 0$ in order to avoid zero or negative i, j, k indexes. i_{mid} and k_{mid} are used to determine the center of mass and the center of our calculation frame at $\boldsymbol{x} = (0, 0, 0)$. The $x = 0$ line locates between the cells with indexes i_{mid} and $i_{mid}{+}1$. The $z = 0$ line locates between the cells with indexes k_{mid} and $k_{mid}{+}1$. The $y = 0$ line just lie on the edges of $j = 1$ cells. Since the negative y-directed cells are not stored in the list, when we calculate some measurable quantities, i.e., the two particle correlation calculation and the Λ polarization, we should not forget to take into account the contribution by the mirror image side. These mirror side cells have the same invariant scalar quantities as positive cells while the 4-vector components take different values:

$$\begin{aligned} q(-x,-y,-z) &= q(x,y,z)\ , \\ \gamma(-x,-y,-z) &= \gamma(x,y,z)\ , \\ v_x(-x,-y,-z) &= -v_x(x,y,z)\ , \\ v_y(-x,-y,-z) &= -v_y(x,y,z)\ , \\ v_z(-x,-y,-z) &= -v_z(x,y,z)\ , \end{aligned} \tag{A.2}$$

where the 4-velocity is $u^\mu = \gamma(1, v_x, v_y, v_z)$ and the spatial velocity $\boldsymbol{v} = (v_x, v_y, v_z)$. The cell with indexes $(i,\ j,\ k)$ always has the corresponding mirror image cell with the indexes $(i,\ j,\ k) \longrightarrow (\ 2i_{mid}{-}i{+}1,\ -j,\ 2k_{mid}{-}k{+}1\ )$.

Appendix B

Entropy calculation in hydro for zero pressure

We assume two subsystems, one is the parton gas and the other is the Bag field. The parton gas is assumed to be an ideal Stefan-Boltzmann gas with $P_p = e_p/3$ where P_p is parton gas pressure and e_p is parton gas energy density. After introducing the Bag model the system will have

$$P = P_p - B \ , \quad \mathrm{e} = e_p + B \ ,$$

where B is Bag constant. By denoting e_B as energy density of the bag, the pressure P is

$$P = \frac{e}{3} - \frac{4}{3}B \ . \tag{B.1}$$

where e is the total energy density ($e = e_p + e_B$). In the Bag model it is possible that $P < 0$ if $e_B = B$; If $P \leq 0$, in the hydro P is taken as $P = 0$ in the PICR code. When the pressure has reached 0, the work done on one Lagrangian cell by its neighbors vanishes, $P\mathrm{d}V = 0$, and the specific energy, $\varepsilon = E/N$ of Lagrangian fluid cell will stay constant

during the expansion:

$$\varepsilon_{\text{cell}} = \varepsilon = \varepsilon_p + \varepsilon_B = \text{constant} \ , \tag{B.2}$$

because the Lagrangian fluid cells contain a fixed number of net-baryon charge. Thus if we assume $P\mathrm{d}V = 0$, the expansion is adiabatic, $ds = ds_p = 0$. From above we conclude that after the pressure dropped to zero the the parameters at time t will become:

$$\varepsilon_t = \varepsilon_0 \ (\text{ energy conservation }) \ , \tag{B.3}$$

$$\gamma_t = \gamma_0 \ (\text{ because } P = 0 \ ) \ , \tag{B.4}$$

$$\sigma_t = \sigma_0 \ (\text{ because } \mathrm{d}S = 0 \text{ and } \mathrm{d}N = 0 \ ) \ , \tag{B.5}$$

where σ is specific entropy density and $\gamma = 1/\sqrt{1-\boldsymbol{v}^2}$. Let us define the $P = 0$ state, as the initial state of an expansion, so the parameters of the Stefan-Boltzmann parton gas and of the total Bag model are:

$$P_{p_0} = B, \ e_{p_0} = 3B, \ e_0 = 4B, \ P_0 = 0 \ .$$

The code calculates the entropy density s_q correctly when pressure is positive. But at a later time (t) when the pressure becomes negative, the hydro code sets the pressure to $P = 0$, and if the bag constant is still equal to B, this would lead to entropy decrease [54]. Thus the values of s_q would be incorrect. Also the temperature (T) calculated this way is wrong.

For the Lagrangian fluid cell, we define the volume per nucleon ν_0 as $\nu_0 = 1/n_0$, where n_0 is the nucleon density in the initial state. Then we have:

$$\varepsilon_{p_0} = 3B\nu_0, \ \varepsilon_{B_0} = B\nu_0, \ \varepsilon_0 = 4B\nu_0 \ . \tag{B.6}$$

The adiabatic flow is defined as follows:

$$\frac{\varepsilon_p(t)}{\varepsilon_{p0}} = \left(\frac{\nu_t}{\nu_0}\right)^{-4/3} , \tag{B.7}$$

so the parton energy at time t is

$$\varepsilon_p(t) = 3B\nu_0 \left(\frac{\nu_t}{\nu_0}\right)^{-4/3} . \tag{B.8}$$

Because of the energy conservation, according to Eqs. (B.2) and (B.6), we have $\varepsilon(t) = \varepsilon_p(t) + \varepsilon_B(t) = \varepsilon_p(0) + \varepsilon_B(0) = 4B\nu_0$ thus

$$\varepsilon_B(t) = B\nu_0 \left(4 - 3\left(\frac{\nu_t}{\nu_0}\right)^{-4/3}\right) . \tag{B.9}$$

The total specific energy is:

$$\varepsilon = T\sigma - P\nu + \mu = T\sigma + \mu \ .$$

Since the expansion process is adiabatic, $dS = dN = 0$ and $P = 0$, so $d\varepsilon = Td\sigma = 0$. At time t_0, $\varepsilon_0 = 4B\nu_0 = T_0\sigma_0 + \mu_0$, so

$$\mu_0 = 4B\nu_0 - T_0\sigma_0 \ .$$

In the above equation, the T_0 and σ_0 are well calculated in the hydro code. Later at time $t > t_0$, $\varepsilon(t) = 4B\nu_0 = T\sigma_0 + \mu$.

For one Lagrangian fluid cell (LFC) in the calculational frame (CF), the expression of the total particle number is:

$$N^{LFC} = n\gamma V_{\rm CF}^{\rm cell} = n_0\gamma_0 V_0^{\rm cell} \quad (\text{ where } \gamma = \gamma_0 \text{ because of Eq. (B.4) }) \ .$$

From energy conservation $\varepsilon(t) = \varepsilon_0$, and $e = e_{\rm CF}/\gamma$, we obtain

$$\varepsilon(t) = \frac{e_{\rm CF}}{n \cdot \gamma} = 4B\nu_0 = \frac{4B}{n_0} \ ,$$

since n is calculated in hydro code, from this equation n_0 can be calculated:

$$n_0 = n \cdot \frac{4B\gamma}{e_{\rm CF}}, \ \text{or} \ \nu_0 = \nu \frac{e_{\rm CF}}{4B\gamma} \ . \tag{B.10}$$

Then if $P = 0$, the contribution from a calculational cell to entropy can be obtained from $N_{LFC} = n\gamma V_{\rm cell}^{\rm CF} = n_0\gamma V_0$ where $V_0 = \frac{n}{n_0} V_{\rm cell}^{\rm CF}$ and n_0 is calculated in Eq. (B.10). The contribution of the $P = 0$ cell to the total entropy is then

$$\triangle S = N_{LFC} \ \sigma_0^*(\nu_0) = n\gamma V_{\rm cell}^{\rm CF} \ \sigma_0^*(\nu_0) \ , \tag{B.11}$$

where we have to calculate $\sigma_0^*(\nu_0)$ from the EoS Eq. (B.1), i.e., $\sigma_0^*(\nu_0) = \sigma_p(n_0, \varepsilon_{p0})$.

In order to keep the EoS Eq. (B.1) consistent at $P = 0$, we have to change $B \to b$, thus the EoS of zero pressure domain becomes $P = (e - 4b)/3$. Thus when $P = 0$, $b = e/4$. After we change the bag constant to a smaller value when dealing with negative pressure cells, the entropy is increasing as time develops. This is physically consistent. In order to be more transparent, we separate the entropy contribution between the $P > 0$ and $P = 0$ cells. We conclude that the zero pressure cells contribute to the entropy production, because at later time, the partons in these cells become dilute, thus the pressure becomes zero.

Appendix C

Numerical vorticity estimate in the PIC method

Let us first consider fluid cells in 3 spatial directions, for the classical case of vorticity. The vorticity is defined as

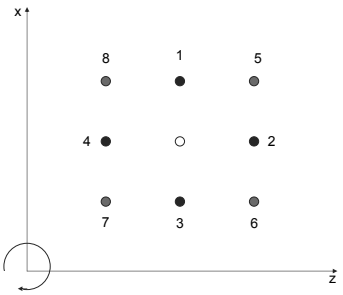

Figure C.1: (color online) The nearest four, side neigbors indicated by $^{+0}$,$^{0+}$,$^{-0}$,$^{0-}$ and the four corner neighbors indicated by $^{++}$,$^{-+}$,$^{--}$,$^{+-}$ of a fluid cell at i, k indicated by ^{00} in the Reaction $[x, z]$ Plane to calculate the partial derivatives. In this section these locations of velocity components and γ factors are indicated by an index number given above.

$$\omega_{zx} \equiv -\omega_{xz} = \frac{1}{2}(\partial_x v_z - \partial_z v_x) \ . \tag{C.1}$$

In this definition the sign convention is opposite to that of the mathematical **rot** operation. Here we use the convention that if the projectile is moving in the positive,

z-direction, and it is at the upper side of the x-direction, and the target is moving the opposite direction, then the vorticity, ω_{zx}, of the flow is positive.

The vorticity at the central point of a fluid cell can be calculated in the following steps. We have a contribution from the side points 1,2,3,4, and for the corner neighbor points 5,6,7,8, see Fig. C.1, so that the vorticity is:

$$\begin{aligned}
-\omega_y \;\equiv\; & \omega_{zx}(i,k) \equiv \frac{1}{2} \times \\
& \left[\left(v_z(i+1,k) - v_z(i,k)\right)/(2\Delta x) \right. \\
+ \;& \left(v_z(i,k) - v_z(i-1,k)\right)/(2\Delta x) \\
- \;& \left(v_x(i,k+1) - v_x(i,k)\right)/(2\Delta z) \\
- \;& \left(v_x(i,k) - v_x(i,k-1)\right)/(2\Delta z) \\
+ \;& \left(v_z(i+1,k+1) - v_z(i,k+1)\right)/(4\Delta x) \\
+ \;& \left(v_z(i,k-1) - v_z(i-1,k-1)\right)/(4\Delta x) \\
+ \;& \left(v_z(i+1,k-1) - v_z(i,k-1)\right)/(4\Delta x) \\
+ \;& \left(v_z(i,k+1) - v_z(i-1,k+1)\right)/(4\Delta x) \\
- \;& \left(v_x(i+1,k+1) - v_x(i+1,k)\right)/(4\Delta z) \\
- \;& \left(v_x(i-1,k) - v_x(i-1,k-1)\right)/(4\Delta z) \\
- \;& \left(v_x(i-1,k+1) - v_x(i-1,k)\right)/(4\Delta z) \\
- \;& \left. \left(v_x(i+1,k) - v_x(i+1,k-1)\right)/(4\Delta z) \right] \; .
\end{aligned} \tag{C.2}$$

Here each of the 12 lines corresponds to an x-directed or z-directed link among the cell and its 8 neighbors. If all cells, also the neighbours are filled with matter with not exactly zero velocity, in each of the above lines one of the two velocity values cancel with another one, thus in the above list only 12 velocities should be evaluated. On the other hand if not all neighbors of a cell are filled with matter, then the *lines* which include an empty cell should be dropped from the list. These are usually the surface cells in a heavy ion collision.

We can also use the shorter notation of the indices - for -1 and + for +1, so that the above equation takes the form:

$$\begin{aligned} -\omega_y \;\equiv\; & \omega_{zx}(i,k) \equiv \frac{1}{2} \times \\ & \left[\left((v_z^{+0} - v_z^{00}) + (v_z^{00} - v_z^{-0})\right)/(2\Delta x)\right. \\ - \;& \left((v_x^{0+} - v_x^{00}) + (v_x^{00} - v_x^{0-})\right)/(2\Delta z) \\ + \;& \left((v_z^{++} - v_z^{0+}) + (v_z^{0-} - v_z^{--}) + (v_z^{+-} - v_z^{0-}) + (v_z^{0+} - v_z^{-+})\right)/(4\Delta x) \\ - \;& \left.\left((v_x^{++} - v_x^{+0}) + (v_x^{-0} - v_x^{--}) + (v_x^{-+} - v_x^{-0}) + (v_x^{+0} - v_x^{+-}\right)/(4\Delta z)\right] \;. \end{aligned} \tag{C.3}$$

Here if all cells are filled with matter in the first two lines the ^{00} cells cancel each other and the last two lines the $^{0-}$,$^{0+}$,$^{-0}$,$^{+0}$ cells would cancel each other. In this situation we could replace the the $^{0-}$,$^{0+}$,$^{-0}$,$^{+0}$ cells with the central ^{00} cell, without changing the result:

$$\begin{aligned} -\omega_y \;\equiv\; & \omega_{zx}(i,k) \equiv \frac{1}{2} \times \\ & \left[\left((v_z^{+0} - v_z^{00}) + (v_z^{00} - v_z^{-0})\right)/(2\Delta x)\right. \\ - \;& \left((v_x^{0+} - v_x^{00}) + (v_x^{00} - v_x^{0-})\right)/(2\Delta z) \\ + \;& \left((v_z^{++} - v_z^{00}) + (v_z^{00} - v_z^{--}) + (v_z^{+-} - v_z^{00}) + (v_z^{00} - v_z^{-+})\right)/(4\Delta x) \\ - \;& \left.\left((v_x^{++} - v_x^{00}) + (v_x^{00} - v_x^{--}) + (v_x^{-+} - v_x^{00}) + (v_x^{00} - v_x^{+-}\right)/(4\Delta z)\right] \;. \end{aligned} \tag{C.4}$$

This would mean that the four corner links would be connected to the central cell. Consequently not all of the links are now axis directed. For a domain where all cells are filled, this gives exactly the same result. We could now drop all terms containing $v_x(i,k)$ and $v_z(i,k)$ if all cells are filled.

For surface cells this cannot be done, because we have to delete each link where there is an empty cell. To replace the empty cell by zero velocity would lead to a large derivative, because neighboring cells have similar velocities (not necessarily close to zero). So we use the above expression for general calculation of the vorticity, eliminating those

lines, (i.e. those links) where one of the cells are empty.

If some cells are empty in the above expression the weights for the remaining cells could be increased. However, in the present calculation we do not do this, we keep Eqs. C.5, and keep the weights the same. We drop the lines, which contain empty cells. This results in somewhat reduced $|\omega_y|$ values in the vicinity of the boundaries, while the result is much more accurate than dropping all cells which would cancel in a densely filled domain.

For the internal cells where all neighbors are filled we can let the central cell cancel in the expression, and for these inside cells we get:

$$\begin{aligned} -\omega_y \equiv \omega_{zx}(i,k) \quad &\equiv \quad \frac{2(v_z^{+0}-v_z^{-0})+v_z^{++}-v_z^{--}+v_z^{+-}-v_z^{-+}}{8\Delta x} \\ &- \quad \frac{2(v_x^{0+}-v_z^{0-})+v_x^{++}-v_x^{--}+v_x^{-+}-v_x^{+-}}{8\Delta z} \ . \end{aligned} \tag{C.5}$$

In relativistic flow: Here for the vorticity development in the Reaction Plane we calculate ω^z_x, using the same convention as above for the classical case:

$$\omega^z_x = \frac{1}{2}(\partial_x \gamma v_z - \partial_z \gamma v_x) = \frac{1}{2}\gamma(\partial_x v_z - \partial_z v_x) + \frac{1}{2}(v_z \partial_x \gamma - v_x \partial_z \gamma) \ . \tag{C.6}$$

The first term is similar to the classical case. It has just to be multiplied by a factor γ, while the second term has a similar structure:

$$\begin{aligned} &\omega^z_x(i,k) \equiv \frac{1}{8} \times \\ &\left[\gamma^{00}\left(2\left((v_z^{+0}-v_z^{00})+(v_z^{00}-v_z^{-0})\right)+(v_z^{++}-v_z^{00})+(v_z^{00}-v_z^{--})+(v_z^{+-}-v_z^{00})+(v_z^{00}-v_z^{-+})\right)/\Delta x\right. \\ -\ &\left.\gamma^{00}\left(2\left((v_x^{0+}-v_x^{00})+(v_x^{00}-v_x^{0-})\right)+(v_x^{++}-v_x^{00})+(v_x^{00}-v_x^{--})+(v_x^{-+}-v_x^{00})+(v_x^{00}-v_x^{+-})\right)/\Delta z\right] \\ +\ &\left[v_z^{00}\left(2\left((\gamma^{+0}-\gamma^{00})+(\gamma^{00}-\gamma^{-0})\right)+(\gamma^{++}-\gamma^{00})+(\gamma^{00}-\gamma^{--})+(\gamma^{+-}-\gamma^{00})+(\gamma^{00}-\gamma^{-+})\right)/\Delta x\right. \\ -\ &\left.v_x^{00}\left(2\left((\gamma^{0+}-\gamma^{00})+(\gamma^{00}-\gamma^{0-})\right)+(\gamma^{++}-\gamma^{00})+(\gamma^{00}-\gamma^{--})+(\gamma^{-+}-\gamma^{00})+(\gamma^{00}-\gamma^{+-})\right)/\Delta z\right] \ . \end{aligned}$$

Just as in the classical case if we have a neighboring cell which is empty, the whole

corresponding link (i.e. $(\gamma-\gamma)$ and $(v-v)$ term) should be dropped from this summation.

In case if all neighboring cells are filled then all q^{00} terms cancel and the expression simplifies considerably:

$$\begin{aligned}
&\omega^z_x(i,k) \equiv \frac{1}{8} \times \\
&\left[\gamma^{00}\left(2\left((v_z^{+0}-v_z^{-0})\right)+(v_z^{++}-v_z^{--})+(v_z^{+-}-v_z^{-+})\right)/\Delta x\right. \\
-\;&\left.\gamma^{00}\left(2\left((v_x^{0+}-v_x^{0-})\right)+(v_x^{++}-v_x^{--})+(v_x^{-+}-v_x^{+-})\right)/\Delta z\right] \\
&\left[v_z^{00}\left(2\left((\gamma^{+0}-\gamma^{-0})\right)+(\gamma^{++}-\gamma^{--})+(\gamma^{+-}-\gamma^{-+})\right)/\Delta x\right. \\
-\;&\left.v_x^{00}\left(2\left((\gamma^{0+}-\gamma^{0-})\right)+(\gamma^{++}-\gamma^{--})+(\gamma^{-+}\gamma^{+-})\right)/\Delta z\right] \ .
\end{aligned} \tag{C.7}$$

Appendix D

Baryon density, momentum of inertia, kinetic energy

Scaling of density distributions

Let us evaluate the baryon density, $n(s)$, and for simplicity we assume that in case 1A of Ref. [47] the temperature is constant, $\mathcal{T}(s) = 1$, then it follows that, $\nu(s) = (N_B/V)\exp(-s/2)$, where $N_B = n_0 V_0$. Due to the exponential density profile, if s is a sum of the coordinates in two orthogonal directions, as $s = s_\rho = s_z$, then n(s) separates into two multiplicative terms: $n_\rho(s_\rho)$ and $n_z(s_z)$. For further simplifying the formalism, we can introduce a coordinate change $s = \frac{1}{2}u$ for integrals of type $\int_0^{U/2} f(u/2)\,du$. Then $ds = \frac{1}{2}\,du$ and $\int_0^{U/2} f(u/2)\,du = 2\int_0^S f(s)\,ds$. This change will thus modify the upper limits of integration, and the normalization by a factor of two. These adjustments are included in the final expressions for the momentum of inertia and the kinetic energy.

The baryon density distribution is then

$$n(r_\rho, r_z) = N_B \frac{C_n}{V} e^{-r_\rho^2/R^2} e^{-r_z^2/Z^2} \ ,$$

where C_n is a normalization constant, which will be determined later.

$$\iint n(r_\rho, r_z) dr_\rho dr_z = N_B \frac{C_n}{V} 2\pi \int_0^{R/\infty} e^{-r_\rho^2/R^2} r_\rho dr_\rho \int_{-Z/\infty}^{Z/\infty} e^{-r_z^2/Z^2} dr_z \ , \tag{D.1}$$

here the first integral up to infinity gives $\Gamma(1)R^2/2$, while the second one $\Gamma(0.5)Z = \sqrt{\pi}Z$. In x, y, z coordinates this is:

$$N_B \frac{C_n}{V} \times \left(\int_{-\infty}^{\infty} e^{-r_x^2/X^2} dr_x \right)^3 = N_B \frac{C_n}{V} \left(\sqrt{\pi} X \right)^3 = N_B \times \text{const.} \ . \tag{D.2}$$

Or in cylindrical coordinates

$$N_B \frac{C_n}{V} \quad \times \quad \pi\Gamma(1)R^2 \times \sqrt{\pi} Z = N_B \frac{C_n}{V} \pi^{3/2} R^2 Z \ , \tag{D.3}$$

which is the same. The integrals were evaluated up to limits in infinity. If we perform the definite integrals up to a finite limit, we get similar scaling behaviour. Let us now change the variables to scaling variables introduced in Ref. [47], but in cylindrical coordinates:

$$n(s_\rho, s_z) = N_B \frac{C_n}{V} e^{-s_\rho/2} e^{-s_z/2} \ .$$

Now using the relations $2\pi r_\rho dr_\rho = \pi R^2 ds_\rho$ and $dr_z = \frac{Z}{2\sqrt{s_z}} ds_z$ we get

$$\begin{aligned} \iint n(s_\rho, s_z) ds_\rho ds_z &= N_B \frac{C_n}{V} \pi R^2 \times \int_0^1 e^{-s_\rho/2} \, ds_\rho \times Z \int_0^1 e^{-s_z/2} \, \frac{ds_z}{\sqrt{s_z}} \\ &= N_B C_n \frac{\pi R^2 Z}{V} 2 \times \int_0^{0.5} e^{-u} \, du \times \sqrt{2} \int_0^{0.5} e^{-u} \, \frac{du}{\sqrt{u}} \\ &= N_B C_n \frac{\pi R^2 Z}{V} \ 2 \, I_A(0.5) \ \sqrt{2} \, I_B(0.5) \ . \end{aligned} \tag{D.4}$$

This should be equal to N_B thus the normalization constant is

$$C_n = 1 \Big/ \left[2\sqrt{2} \, I_A(0.5) \, I_B(0.5) \right] \ .$$

Here $I_A(0.5)$ and $I_B(0.5)$ are constants, which do not change during the scaling evolution, when the density profile remains the same. At infinity $I_A(\infty) = \Gamma(1)$, while $I_B(\infty) = \Gamma(0.5) = \sqrt{\pi}$, but at different integration limits the ratio of the two integrals will be different [55]:

$$\begin{aligned} I_A(u) &= 1 - \exp(-u) \ , \\ I_B(u) &= \sqrt{\pi}\, \Phi(\sqrt{u}\,) \ , \end{aligned} \tag{D.5}$$

where

$$\Phi(u) = \mathrm{erf}(u) \equiv \frac{2}{\sqrt{\pi}} \int_0^u \exp(-x^2)\, dx \ . \tag{D.6}$$

The Moment of Inertia

Consider a body with scaling expansion, and with solid body rotation (i.e. the angular velocity is uniform for the whole body, $\omega = \omega(t)$ but it does not depend on the spatial coordinates. Let us denote the moment of inertia with Θ:

$$\Theta = \int m\, n(r)\, r^2\, d^3r \ . \tag{D.7}$$

Then the angular momentum and the rotational energy are

$$L = \Theta\omega \quad \text{and} \quad E = \frac{1}{2}\Theta\omega^2 \ . \tag{D.8}$$

Now we assume that our system has no external torque, and all internal forces are radial, so the angular momentum must be conserved, during the scaling expansion driven by the pressure gradient which is radial in a cylindrically symmetric system. Thus, the angular velocity is not directly influenced by the dynamics, just via the angular momentum

conservation. From $\dot{L} = 0$, it follows that

$$\dot{\Theta}\omega = -\Theta\dot{\omega} \quad \text{or} \quad \dot{\omega} = -\omega\frac{\dot{\Theta}}{\Theta} \ .$$

Thus the change of the angualr velocity is a direct consequence of the change of the moment of inertia Θ, while Θ is proportional with the square of the radius of the system in a scaling expansion where the density profile remains the same during the expansion. Consequently

$$\dot{\omega} \ = \ -\omega\frac{\dot{\Theta}}{\Theta} \ = \ -\omega\frac{\dot{R}^2}{R^2} \quad \text{and} \quad \omega \ = \ \omega_0\frac{R_0}{R} \ .$$

We still have to evaluate the moment of inertia accurately to provide precisely the energy of rotation. Thus by using the scaling variables we have:

$$\begin{aligned} \Theta &= mN_B\frac{\pi R^2\, Z}{V}R^2C_n\int_0^1 e^{-s_\rho/2}s_\rho ds_\rho \times \int_0^1 e^{-s_z/2}\frac{ds_z}{\sqrt{s_z}} \\ &= m\, N_B\, R^2\ C_n\ 4\, I_C(0.5)\,\sqrt{2}\, I_B(0.5) \ , \end{aligned} \tag{D.9}$$

where $I_C(u) = 1 - (1+u)\exp(-u)$.

As before these integrals do not change during the scaling expansion, on the other hand the volume and the moment of inertia have different coefficients in the energy expression. As a consequence the kinetic energy of the rotation is

$$\begin{aligned} E_K &= \frac{1}{2}\Theta\omega^2 = \frac{1}{2}m\, N_B\ C_n 4\sqrt{2}\, I_C(0.5)\, I_B(0.5)\, R^2\omega^2 \\ &= \frac{1}{2}\alpha^2\, m\, N_B\ R^2\omega^2 \ . \end{aligned} \tag{D.10}$$

Here we have itroduced the constant

$$\alpha^2 \equiv 4\sqrt{2}\, C_n I_B(\frac{1}{2}) I_C(\frac{1}{2}) \ , \tag{D.11}$$

which can be used in the main course of the work.

Kinetic energy of radial and longitudinal expansion

The radial velocity is given by $v_\rho = (\dot{R}/R)r_\rho$ and consequently $v_\rho^2 = \dot{R}^2 s_\rho$. Thus the kinetic energy of radial expansion is

$$\begin{aligned} E_K &= \frac{mN_B}{2}\frac{\pi R^2 Z}{V}\dot{R}^2 C_n \int_0^1 e^{-s_\rho/2} s_\rho ds_\rho \int_0^1 e^{-s_z/2}\frac{ds_z}{\sqrt{s_z}} \\ &= \frac{mN_B}{2} C_n 4\sqrt{2}\, I_C(0.5)\, I_B(0.5)\ \dot{R}^2 \\ &= \frac{mN_B}{2}\,\alpha^2\ \dot{R}^2\ . \end{aligned} \tag{D.12}$$

The longitudinal velocity is given by $v_z = (\dot{Z}/Z)r_z$ and consequently $v_z^2 = \dot{Z}^2 s_z$. Thus the kinetic energy of longitudinal expansion is

$$\begin{aligned} E_K &= \frac{mN_B}{2}\frac{\pi R^2 Z}{V}\dot{Z}^2 C_n \int_0^1 e^{-s_\rho/2} ds_\rho \int_0^1 e^{-s_z/2}\sqrt{s_z} ds_z \\ &= \frac{mN_B}{2} C_n\ 4\sqrt{2}\, I_A(0.5)\, I_D(0.5)\ \dot{Z}^2\ , \end{aligned} \tag{D.13}$$

where $I_D(u) = \frac{\sqrt{\pi}}{2}\Phi(\sqrt{u}) - \sqrt{u}e^{-u}$. Here we can introduce the constant

$$\beta^2 \equiv 4\sqrt{2}\, C_n I_A(\frac{1}{2}) I_D(\frac{1}{2})\ , \tag{D.14}$$

which will be used in the calculation.

Appendix E

Correlation function for fluid cells

We use the thermal velocity $\boldsymbol{\beta}_s \equiv \boldsymbol{u}_s/T_s$, and consider each cell with index $j = 1$ has a corresponding mirror image cell with position $j = -1$. The indexes of fluid cells are introduced in Appendix A. Fig. E.1 shows the cells placed symmetrically around the origin of the Descartes coordinate system in the reaction, [x,z]-plane. All the cells and their mirror image cells have equal scalar parameters while the vectors are different: The cell in the top layer ($x > 0$) have thermal velocity $\boldsymbol{\beta}_s$, while it is $-\boldsymbol{\beta}_s$ for the bottom layer. The coordinates of the two corresponding mirror symmetry cell centers are $(\pm x_s, \pm y_s, \pm z_s)$. The weights are not necessarily the same: $w_s(j > 0) \neq w_s^*(j < 0)$, where the symbol * denotes the parameter for the mirror cell.

Two fluid cells

Here we show how to calculate the correlation function for the two cells marked by the red circles in Fig. E.1. First we calculate the integral of function $S(k, q)$:

$$\int d^4x\, S(x,k) = \left(2\pi R^2\right)^{3/2} P_s \left[w_s \exp\left(\boldsymbol{k}\boldsymbol{\beta}_s\right) + w_s^* \exp\left(-\boldsymbol{k}\boldsymbol{\beta}_s\right)\right], \tag{E.1}$$

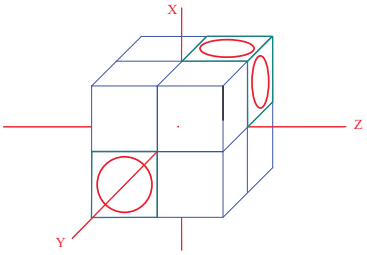

Figure E.1: (color online) Eight fluid cells placed symmetrically around the origin of the Descartes coordinate system. The cells on the negative y-side of the coordinate space (further away from us) are reflected around the point of origin (c.m.) and are not calculated explicitly in the fluid dynamical model. The top layer has uniform velocity pointing to the right (positive z-direction), while the bottom layer has a uniform velocity to the opposite direction. Random fluctuations would violate this exact symmetry. For two fluid cells in the calculation we only consider the two fluid cells marked by the red circles.

thus the denominator in Eq. (5.7) is

$$\left|\int d^4x\, S(x,k)\right|^2 = \left(2\pi R^2\right)^3 P_s^2 \quad \left[w_s^2 \exp\left(2\boldsymbol{k}\boldsymbol{\beta}_s\right) + (w_s^*)^2 \exp\left(-2\boldsymbol{k}\boldsymbol{\beta}_s\right) + 2w_s w_s^*\right]. \quad \text{(E.2)}$$

In order to get the nominator of Eq. (5.7), we first calculate the $J(k,q)$ function according to Eqs. (5.15):

$$J(k,q) = \; Q_c P_s Q_s^q \left[w_s e^{\boldsymbol{k}\boldsymbol{\beta}_s}\, e^{\boldsymbol{q}\boldsymbol{\beta}_s/2} e^{i\boldsymbol{q}\boldsymbol{x}_s} + w_s^* e^{-\boldsymbol{k}\boldsymbol{\beta}_s}\, e^{-\boldsymbol{q}\boldsymbol{\beta}_s/2} e^{-i\boldsymbol{q}\boldsymbol{x}_s}\right] , \quad \text{(E.3)}$$

where $\boldsymbol{x}_s$ is the position of the center of the cell on the positive y side, while the mirror image cell has $-\boldsymbol{x}_s$. In the above expression we can insert

$$e^{i\boldsymbol{q}\boldsymbol{x}_s} = \cos(\boldsymbol{q}\boldsymbol{x}_s) + i\sin(\boldsymbol{q}\boldsymbol{x}_s) \quad \text{(E.4)}$$

and we introduce the notations $\Sigma(\boldsymbol{q}) = e^{i\boldsymbol{q}\boldsymbol{x}_s}$, thus we have

$$\Sigma(\boldsymbol{q}) = \; \cos \boldsymbol{q}\boldsymbol{x}_s + i \sin \boldsymbol{q}\boldsymbol{x}_s. \quad \text{(E.5)}$$

Notice that $Re[\Sigma^2(\boldsymbol{q})] = Re[\Sigma^2(-\boldsymbol{q})] = C_q^2 - S_q^2$ and $Re[\Sigma(\boldsymbol{q})\Sigma(-\boldsymbol{q})] = C_q^2 + S_q^2$, where $C_q = \cos \boldsymbol{q}\boldsymbol{x}_s$, and $S_q = \sin \boldsymbol{q}\boldsymbol{x}_s$.

Using this substitution the $Re[J(k,q)J(k,-q)]$ product becomes:

$$
\begin{aligned}
Re[J(k,q)J(k,-q)] = \; & (Q_c P_s)^2 \times \\
Re\Big[& \Big(w_s e^{\boldsymbol{k}\boldsymbol{\beta}_s} e^{\boldsymbol{q}\boldsymbol{\beta}_s/2} \Sigma(\boldsymbol{q}) + w_s^* e^{-\boldsymbol{k}\boldsymbol{\beta}_s} e^{-\boldsymbol{q}\boldsymbol{\beta}_s/2} \Sigma(-\boldsymbol{q}) \Big) \times \\
& \Big(w_s e^{\boldsymbol{k}\boldsymbol{\beta}_s} e^{-\boldsymbol{q}\boldsymbol{\beta}_s/2} \Sigma(-\boldsymbol{q}) + w_s^* e^{-\boldsymbol{k}\boldsymbol{\beta}_s} e^{\boldsymbol{q}\boldsymbol{\beta}_s/2} \Sigma(\boldsymbol{q}) \Big) \Big] = \\
& (Q_c P_s)^2 \times \\
Re\Big[& \; w_s^2 e^{\boldsymbol{k}\boldsymbol{\beta}_s} e^{\boldsymbol{q}\boldsymbol{\beta}_s/2} \; e^{\boldsymbol{k}\boldsymbol{\beta}_s} e^{-\boldsymbol{q}\boldsymbol{\beta}_s/2} \; \Sigma(\boldsymbol{q})\Sigma(-\boldsymbol{q}) + \\
& w_s \, w_s^* \, e^{\boldsymbol{k}\boldsymbol{\beta}_s} e^{\boldsymbol{q}\boldsymbol{\beta}_s/2} \; e^{-\boldsymbol{k}\boldsymbol{\beta}_s} e^{\boldsymbol{q}\boldsymbol{\beta}_s/2} \; \Sigma^2(\boldsymbol{q}) + \\
& w_s^* \, w_s \, e^{-\boldsymbol{k}\boldsymbol{\beta}_s} e^{-\boldsymbol{q}\boldsymbol{\beta}_s/2} \; e^{\boldsymbol{k}\boldsymbol{\beta}_s} e^{-\boldsymbol{q}\boldsymbol{\beta}_s/2} \; \Sigma^2(-\boldsymbol{q}) + \\
& (w_s^*)^2 e^{-\boldsymbol{k}\boldsymbol{\beta}_s} e^{-\boldsymbol{q}\boldsymbol{\beta}_s/2} \; e^{-\boldsymbol{k}\boldsymbol{\beta}_s} e^{\boldsymbol{q}\boldsymbol{\beta}_s/2} \; \Sigma(-\boldsymbol{q})\Sigma(\boldsymbol{q}) \Big] = \\
& (Q_c P_s)^2 \times \\
Re\Big[& w_s^2 e^{2\boldsymbol{k}\boldsymbol{\beta}_s} \; \Sigma(\boldsymbol{q})\Sigma(-\boldsymbol{q}) + w_s \, w_s^* \, e^{\boldsymbol{q}\boldsymbol{\beta}_s} \; \Sigma^2(\boldsymbol{q}) + \\
& w_s \, w_s^* \, e^{-\boldsymbol{q}\boldsymbol{\beta}_s} \; \Sigma^2(-\boldsymbol{q}) + (w_s^*)^2 \, e^{-2\boldsymbol{k}\boldsymbol{\beta}_s} \; \Sigma(-\boldsymbol{q})\Sigma(\boldsymbol{q}) \Big] = \\
(Q_c P_s)^2 \Big[& 2 \, w_s \, w_s^* \, \cosh(\boldsymbol{q}\boldsymbol{\beta}_s) \, (C_q^2 - S_q^2) + \\
& \Big(w_s^2 e^{2\boldsymbol{k}\boldsymbol{\beta}_s} + (w_s^*)^2 e^{-2\boldsymbol{k}\boldsymbol{\beta}_s} \Big) \; (C_q^2 + S_q^2) \Big] \; .
\end{aligned}
$$

Here we use the the fact that $Q_s^q \, Q_s^{-q}$ reduces to unity in the product $J(k,q) \, J(k,-q)$. This is also true for eight and all cells. Thus the correlation function becomes:

$$
C(k,q) = 1 + \exp(-R^2 q^2) \times \\
\frac{2 \, w_s \, w_s^* \, \cosh(\boldsymbol{q}\boldsymbol{\beta}_s) \, (C_q^2 - S_q^2) + \Big[w_s^2 e^{2\boldsymbol{k}\boldsymbol{\beta}_s} + (w_s^*)^2 e^{-2\boldsymbol{k}\boldsymbol{\beta}_s} \Big] \; (C_q^2 + S_q^2)}{w_s^2 \exp(2\boldsymbol{k}\boldsymbol{\beta}_s) + (w_s^*)^2 \exp(-2\boldsymbol{k}\boldsymbol{\beta}_s) + 2 w_s w_s^*} \; . \tag{E.6}
$$

Due to the symmetric configuration the coefficients $(C_q^2 + S_q^2)$ and $(C_q^2 - S_q^2)$ could be simplified further. This is also true for eight and all fluid cells.

Eight fluid cells

Now we need to calculate the correlation function for all the eight cells shown in Fig. E.1. Similarly to the two fluid cell calculation, the integral of the source function $S(k,q)$ is

$$\begin{aligned}\int d^4x\, S(x,k) &= \left(2\pi R^2\right)^{3/2} \sum_{s=1}^{4} P_s w_s \left[\exp\left(\boldsymbol{k\beta}\right) + \exp\left(-\boldsymbol{k\beta}\right)\right] \\ &= 4\left(2\pi R^2\right)^{3/2} P_s w_s \left[\exp\left(\boldsymbol{k\beta}\right) + \exp\left(-\boldsymbol{k\beta}\right)\right] \\ &= 8\left(2\pi R^2\right)^{3/2} P_s w_s \cosh\left(\boldsymbol{k\beta}\ \right)\ .\end{aligned} \tag{E.7}$$

Thus denominator is:

$$\left|\int d^4x\, S(x,k)\right|^2 = 64\left(2\pi R^2\right)^3 P_s^2 w_s^2 \cosh(2\boldsymbol{k\beta})\ , \tag{E.8}$$

and the function $J(k,q)$ becomes

$$\begin{aligned}J(k,q) =& Q_c \sum_{s=1}^{4} P_s \left[Q_s^q w_s \exp\left[\left(\boldsymbol{k}+\frac{\boldsymbol{q}}{2}\right)\frac{\boldsymbol{u}_s}{T_s}\right] e^{i\boldsymbol{q}\boldsymbol{x}_s} + Q_s^q w_s^* \exp\left[\left(\boldsymbol{k}+\frac{\boldsymbol{q}}{2}\right)\frac{\boldsymbol{u}_s^*}{T_s}\right] e^{i\boldsymbol{q}\boldsymbol{x}_s^*}\right] \\ &= Q_c P_s Q_s^q w_s \left\{e^{\boldsymbol{k\beta}} e^{\boldsymbol{q\beta}/2}\left[e^{i\boldsymbol{q}\boldsymbol{x}_a} + e^{i\boldsymbol{q}\boldsymbol{x}_b} + e^{i\boldsymbol{q}\boldsymbol{x}_c} + e^{i\boldsymbol{q}\boldsymbol{x}_d}\right]\right. \\ &\left. + e^{-\boldsymbol{k\beta}} e^{-\boldsymbol{q\beta}/2}\left[e^{-i\boldsymbol{q}\boldsymbol{x}_a} + e^{-i\boldsymbol{q}\boldsymbol{x}_b} + e^{-i\boldsymbol{q}\boldsymbol{x}_c} + e^{-i\boldsymbol{q}\boldsymbol{x}_d}\right]\right\}\ ,\end{aligned}$$

where $\boldsymbol{x}_a$, $\boldsymbol{x}_b$, $\boldsymbol{x}_c$, $\boldsymbol{x}_d$ are the positions of the 4 cell centers in the top layer, while the bottom layer has the mirror image cells. Then we introduce the notations as done similar with two cells situations: $\Sigma(\boldsymbol{q}) = e^{i\boldsymbol{q}\boldsymbol{x}_a} + e^{i\boldsymbol{q}\boldsymbol{x}_b} + e^{i\boldsymbol{q}\boldsymbol{x}_c} + e^{i\boldsymbol{q}\boldsymbol{x}_d}$ Thus we can get:

$$\begin{aligned}\Sigma(\boldsymbol{q}) = &\cos\boldsymbol{q}\boldsymbol{x}_a + \cos\boldsymbol{q}\boldsymbol{x}_b + \cos\boldsymbol{q}\boldsymbol{x}_c + \cos\boldsymbol{q}\boldsymbol{x}_d + \\ &i\left[\sin\boldsymbol{q}\boldsymbol{x}_a + \sin\boldsymbol{q}\boldsymbol{x}_b + \sin\boldsymbol{q}\boldsymbol{x}_c + \sin\boldsymbol{q}\boldsymbol{x}_d\right]\ .\end{aligned} \tag{E.9}$$

Notice that $Re[\Sigma^2(\boldsymbol{q})] = Re[\Sigma^2(-\boldsymbol{q})] = C_q^2 - S_q^2$ and $Re[\Sigma(\boldsymbol{q})\Sigma(-\boldsymbol{q})] = C_q^2 + S_q^2$, where C_q and S_q are

$$\begin{aligned} C_q &= \cos \boldsymbol{q}\boldsymbol{x}_a + \cos \boldsymbol{q}\boldsymbol{x}_b + \cos \boldsymbol{q}\boldsymbol{x}_c + \cos \boldsymbol{q}\boldsymbol{x}_d \ , \\ S_q &= \sin \boldsymbol{q}\boldsymbol{x}_a + \sin \boldsymbol{q}\boldsymbol{x}_b + \sin \boldsymbol{q}\boldsymbol{x}_c + \sin \boldsymbol{q}\boldsymbol{x}_d \ . \end{aligned}$$

By using this substitution, the $Re[J(k,q)J(k,-q)]$ product takes the form:

$$\begin{aligned} &Re[J(k,q)J(k,-q)] = \ (Q_c P_s w_s)^2 \times \\ &Re\left[\left(e^{\boldsymbol{k}\boldsymbol{\beta}} e^{\boldsymbol{q}\boldsymbol{\beta}/2}\Sigma(\boldsymbol{q}) + e^{-\boldsymbol{k}\boldsymbol{\beta}} e^{-\boldsymbol{q}\boldsymbol{\beta}/2}\Sigma(-\boldsymbol{q})\right) \times \right. \\ &\left.\left(e^{\boldsymbol{k}\boldsymbol{\beta}} e^{-\boldsymbol{q}\boldsymbol{\beta}/2}\Sigma(-\boldsymbol{q}) + e^{-\boldsymbol{k}\boldsymbol{\beta}} e^{\boldsymbol{q}\boldsymbol{\beta}/2}\Sigma(\boldsymbol{q})\right)\right] = \\ &(Q_c P_s w_s)^2 \times \\ &Re\Big[e^{\boldsymbol{k}\boldsymbol{\beta}} e^{\boldsymbol{q}\boldsymbol{\beta}/2}\ e^{\boldsymbol{k}\boldsymbol{\beta}} e^{-\boldsymbol{q}\boldsymbol{\beta}/2}\ \Sigma(\boldsymbol{q})\Sigma(-\boldsymbol{q}) + \\ &\quad e^{\boldsymbol{k}\boldsymbol{\beta}} e^{\boldsymbol{q}\boldsymbol{\beta}/2}\ e^{-\boldsymbol{k}\boldsymbol{\beta}} e^{\boldsymbol{q}\boldsymbol{\beta}/2}\ \Sigma^2(\boldsymbol{q}) + \\ &\quad e^{-\boldsymbol{k}\boldsymbol{\beta}} e^{-\boldsymbol{q}\boldsymbol{\beta}/2}\ e^{\boldsymbol{k}\boldsymbol{\beta}} e^{-\boldsymbol{q}\boldsymbol{\beta}/2}\ \Sigma^2(-\boldsymbol{q}) + \\ &\quad e^{-\boldsymbol{k}\boldsymbol{\beta}} e^{-\boldsymbol{q}\boldsymbol{\beta}/2}\ e^{-\boldsymbol{k}\boldsymbol{\beta}} e^{\boldsymbol{q}\boldsymbol{\beta}/2}\ \Sigma(-\boldsymbol{q})\Sigma(\boldsymbol{q})\Big] = \\ &(Q_c P_s w_s)^2 \times \\ &Re\Big[e^{2\boldsymbol{k}\boldsymbol{\beta}}\ \Sigma(\boldsymbol{q})\Sigma(-\boldsymbol{q}) + e^{\boldsymbol{q}\boldsymbol{\beta}}\ \Sigma^2(\boldsymbol{q}) + \\ &\quad e^{-\boldsymbol{q}\boldsymbol{\beta}}\ \Sigma^2(-\boldsymbol{q}) + e^{-2\boldsymbol{k}\boldsymbol{\beta}}\ \Sigma(-\boldsymbol{q})\Sigma(\boldsymbol{q})\Big] = \\ &2\,(Q_c P_s w_s)^2 \times \\ &\left[\cosh(2\boldsymbol{k}\boldsymbol{\beta})(C_q^2 + S_q^2) + \cosh(\boldsymbol{q}\boldsymbol{\beta})(C_q^2 - S_q^2)\right] \ . \end{aligned} \tag{E.10}$$

Thus the correlation function becomes:

$$C(k,q) = 1 + \exp(-R^2 q^2)\frac{\left[\cosh(2\boldsymbol{k}\boldsymbol{\beta})(C_q^2 + S_q^2) + \cosh(\boldsymbol{q}\boldsymbol{\beta})(C_q^2 - S_q^2)\right]}{32\cosh(2\boldsymbol{k}\boldsymbol{\beta})} \ . \tag{E.11}$$

All fluid cell pairs

This is the general situation and only the mirror symmetry around the c.m. point of the participant are assumed. This is generally true if the random fluctuations are neglected. Similarly to the previous calculation, we first do the integral for function $S(k,q)$:

$$\int d^4x\, S(x,k) = \left(2\pi R^2\right)^{3/2} \sum_s P_s \mathcal{K}_s \ , \tag{E.12}$$

where

$$\mathcal{K}_s \equiv \left[w_s \exp\left(\boldsymbol{k}\boldsymbol{\beta}_s\right) + w_s^* \exp\left(-\boldsymbol{k}\boldsymbol{\beta}_s\right)\right] \ . \tag{E.13}$$

The denominator in the correlation function is then

$$\left|\int d^4x\, S(x,k)\right|^2 = \left(2\pi R^2\right)^3 \left[\sum_s P_s^2\, \mathcal{K}_s^2 + 2\sum_{s>s'} P_s P_{s'} \mathcal{K}_s \mathcal{K}_{s'}\right] \ . \tag{E.14}$$

The function $J(k,q)$ becomes

$$J(k,q) = Q_c \sum_s P_s Q_s^{(q)} \left[w_s e^{(\boldsymbol{k}+\frac{\boldsymbol{q}}{2})\boldsymbol{\beta}_s + i\boldsymbol{q}\boldsymbol{x}_s} + w_s^* e^{-(\boldsymbol{k}+\frac{\boldsymbol{q}}{2})\boldsymbol{\beta}_s - i\boldsymbol{q}\boldsymbol{x}_s}\right] \ .$$

By substituting the Eq. (E.4), the function $J(k,q)$ become

$$\begin{aligned} J(k,q) &= Q_c \sum_s P_s Q_s^{(q)} \left[\mathcal{C}_s^{(q)} + i\, \mathcal{S}_s^{(q)}\right] \ , \qquad (E.15) \\ \text{where} \quad \mathcal{C}_s^{(q)} &= \left[w_s e^{(\boldsymbol{k}+\frac{\boldsymbol{q}}{2})\boldsymbol{\beta}_s} + w_s^* e^{-(\boldsymbol{k}+\frac{\boldsymbol{q}}{2})\boldsymbol{\beta}_s}\right] \cos(\boldsymbol{q}\boldsymbol{x}_s) \ , \\ \text{and} \quad \mathcal{S}_s^{(q)} &= \left[w_s e^{(\boldsymbol{k}+\frac{\boldsymbol{q}}{2})\boldsymbol{\beta}_s} - w_s^* e^{-(\boldsymbol{k}+\frac{\boldsymbol{q}}{2})\boldsymbol{\beta}_s}\right] \sin(\boldsymbol{q}\boldsymbol{x}_s) \ . \end{aligned}$$

Using this substitution the $Re[J(k,q)J(k,-q)]$ product becomes:

$$\begin{aligned} Re[J(k,q)J(k,-q)] = Q_c^2 \times \\ Re\left[\left(\sum_s P_s Q_s^{(q)}\left[\mathcal{C}_s^{(q)} + i\,\mathcal{S}_s^{(q)}\right]\right)\left(\sum_{s'} P_s Q_{s'}^{(-q)}\left[\mathcal{C}_{s'}^{(-q)} + i\,\mathcal{S}_{s'}^{(-q)}\right]\right)\right] = \\ Q_c^2\left(\sum_s P_s^2\left[\mathcal{C}_s^{(q)}\mathcal{C}_s^{(-q)} - \mathcal{S}_s^{(q)}\mathcal{S}_s^{(-q)}\right]\right. \\ \left. +2\sum_{s>s'} P_s P_{s'} Q_s^{(q)} Q_{s'}^{(-q)}\left[\mathcal{C}_s^{(q)}\mathcal{C}_{s'}^{(-q)} - \mathcal{S}_s^{(q)}\mathcal{S}_{s'}^{(-q)}\right]\right) . \end{aligned} \tag{E.16}$$

Thus the correlation function becomes:

$$C(k,q) = 1 + \exp(-R^2 q^2) \times \frac{\sum_s P_s^2\left[\mathcal{C}_s^{(q)}\mathcal{C}_s^{(-q)} - \mathcal{S}_s^{(q)}\mathcal{S}_s^{(-q)}\right] + 2\sum_{s>s'} P_s P_{s'} Q_s^{(q)} Q_{s'}^{(-q)}\left[\mathcal{C}_s^{(q)}\mathcal{C}_{s'}^{(-q)} - \mathcal{S}_s^{(q)}\mathcal{S}_{s'}^{(-q)}\right]}{\sum_s P_s^2 \mathcal{K}_s^2 + 2\sum_{s>s'} P_s P_{s'} \mathcal{K}_s \mathcal{K}_{s'}} . \tag{E.17}$$

For one pair of fluid cells this expression returned the correlations function expression given in Eq. (57) of Ref. [52].

In this Appendix we present a method, which can exploit the global symmetry of a heavy ion collision across the c.m. point. The formulae for the evaluation include summations over cell-pairs and the correlations between any of the cells with any other cells are also included in the summation.

Weight of the cell as emission source

The weight factor w_s is important when all the fluid cells are considered as emission sources in the hydro model.

For test we first assume that the weight is the same for all directions of $\boldsymbol{k}$ which means for the mirror image cells $w_s^* = w_s$, if $\Theta_s^2(\boldsymbol{x}_s)$ is the same for both. Nevertheless, the factors $\exp[\boldsymbol{ku}/T_s]$ in the $\mathcal{K}$, $\mathcal{C}_s^{(q)}$, and$\mathcal{S}_s^{(q)}$-functions will give strong dominance for the fluid cells, which move towards $\boldsymbol{k}$. In this case the correlation function only includes

cos and cosh terms, see Eq. (63) in Ref. [52], thus the velocity vector does not influence the correlation function, it depends only on the scalar value of the velocities. If the weights are not the same, the correlation function will contain sinh terms also which may contribute differently for the mirror cells. This is shown by Eq. (66) of Ref. [52].

Then we choose the most frequently used approach that we assume the FO hypersurface lay along a constant proper time hyperboloid. Thus we can choose the time-like FO normal as $\hat{\sigma}_{s\mu} = (\gamma_s, \boldsymbol{u}_s)$ and we have $(k_\mu \hat{\sigma}_s^\mu) = \gamma_s k_0 + \boldsymbol{k}\boldsymbol{u}_s$, so the weight becomes

$$w_s = (\gamma_s k_0 + \boldsymbol{k}\boldsymbol{u}_s)\ \exp(-\Theta^2 q_0^2/2) \quad \text{for positive j cells ,} \tag{E.18}$$

$$w_s^* = (\gamma_s k_0 - \boldsymbol{k}\boldsymbol{u}_s)\ \exp(-\Theta^2 q_0^2/2) \quad \text{for mirror cells .} \tag{E.19}$$

As we can see the weights are explicitly different for the cell and its mirror image cell This definition makes the correlation function asymmetric and sensitive to the direction of the rotation of the flow. In Refs. [56, 57] more sophisticated parametrizations are discussed.

Appendix F

Publications

Publications in Scientific Journals

1. Vorticity in peripheral collisions at the FAIR and the NICA

   L.P. Csernai, D.J. Wang, M. Bleicher and H. Stöcker

   Phys. Rev. C **90**, 021904(R) (2014)

2. Rotation in an exact hydrodynamical model

   L.P. Csernai, D.J. Wang and T. Csörgő

   Phys. Rev. C **90**, 024901 (2014)

3. New method to detect rotation in high-energy heavy-ion collisions

   L.P. Csernai, S. Velle and D.J. Wang

   Phys. Rev. C **89**, 034916 (2014)

4. Λ polarization in peripheral heavy ion collisions

   F. Becattini, L.P. Csernai and D.J. Wang

   Phys. Rev. C **88**, 034905 (2013)

5. Viscous potential flow analysis of peripheral heavy ion collisions

   D.J. Wang, Z. Néda and L.P. Csernai

   Phys. Rev. C **87**, 024908 (2013)

6. Flow vorticity in peripheral high-energy heavy-ion collisions
   L.P. Csernai, V.K. Magas, D. J. Wang
   Phys. Rev. C **87**, 034906 (2013)

7. QGP flow fluctuations and the characteristics of higher moments
   D.J. Wang, L.P. Csernai, D. Strottman, Cs. Anderlik, Y. Cheng,
   D.M. Zhou, Y.L. Yan, X. Cai and B.H. Sa
   Eur. Phys. J. A **48**: 168 (2012)
   http://dx.doi.org/10.1140/epja/i2012-12168-4

Publications in Peer Reviewed Conference Proceedings

8. Differential HBT method to analyze rotation in heavy-ion collisions
   L.P. Csernai, S. Velle and D.J. Wang
   Nucl. Phys. A (2014)
   http://dx.doi.org/10.1016/j.nuclphysa.2014.08.028

9. Rotation and turbulent instability in peripheral heavy ion collisions
   L.P. Csernai and D.J. Wang
   EPJ Web of Conferences **71**, 00029 (2014)
   http://dx.doi.org/10.1051/epjconf/20147100029

10. Turbulence, vorticity and Lambda polarization
    L.P. Csernai, F. Becattini and D.J. Wang
    Journal of Physics: Conference Series **509**, 012054 (2014)
    http://dx.doi.org/10.1088/1742-6596/509/1/012054

11. Directed flow from global symmetry and initial state fluctuations
    L.P. Csernai, A.M. Skålvik, D.J. Wang,D. Strottman, C. Anderlik,
    Y. Cheng, Y.L. Yan and B.H. Sa
    Cent. Eur. J. Phys. **10**, 1271-1273 (2012).

12. Flow components and initial state c.m. fluctuations

    L.P. Csernai, A.M. Skålvik, D.J. Wang, V.K. Magas, H. Stöcker,

    D.D. Strottman, Y. Cheng and Y.L. Yan

    Acta Phys. Polonica B **43**, 803 (2012).

Manuscript in preparation

13. Lambda polarization in peripheral intermediate energy heavy ion collisions

    L.P. Csernai, D.J. Wang and F. Becattini

    In preparation (the manuscript is not included in the thesis)